

Hydrothermal Synthesis of Euhedral Co_3O_4 Nanocrystals via Nutrient-Assisted Topotactic Transformation of the Layered $\text{Co}(\text{OH})_2$ Precursor under Anoxic Conditions: Insights into Intricate Routes Leading to Spinel Phase Development and Shape Perfection

Joanna Gryboś,* Camillo Hudy, Angelika Gryczynska, Witold Piskorz, and Zbigniew Sojka*



Cite This: *Cryst. Growth Des.* 2020, 20, 7771–7787



Read Online

ACCESS |



Metrics & More

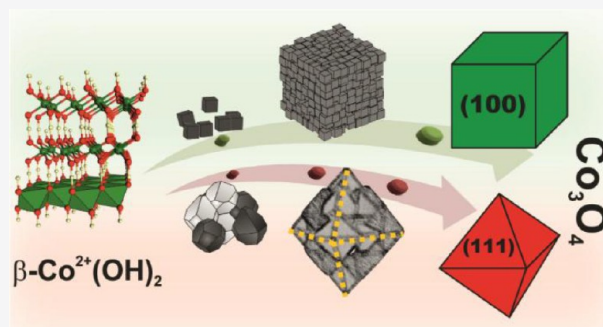


Article Recommendations



Supporting Information

ABSTRACT: Euhedral cobalt spinel cubes, octahedra, and cuboctahedra with narrow size dispersions have been synthesized in a one-pot hydrothermal reaction, using cobalt(II) nitrate and sodium hydroxide at variable concentrations as the only reagents, while their ratio was kept constant at $c_{\text{Co}^{2+}}/c_{\text{OH}^-} = 2.7$. Three main reaction stages, including parent reactive template (PRT) formation, nutrient-mediated topotactic nucleation (NTN), and morphogenesis of nanocrystals (MNC), were distinguished. In the NTN step, the primary spinel grains development occurs with the $[100]$ and $[111]$ directions of the Co_3O_4 facets inheriting the $[1-11]$ direction of the elongated PRT plates (formation of cubes) or the $[001]$ direction of the hexagonal PRT plates (formation of octahedra). In an anoxic environment, the excess nitrate anions play a critical role as the Co^{2+} to Co^{3+} oxidants and oxygen donors required to attain the Co_3O_4 stoichiometry. The nucleated Co_3O_4 primary nanocrystals are spontaneously assembled into sub-micrometer spinel mesocrystals via imperfectly oriented attachments and then consolidated into euhedral bulk nanocrystals by a hydrothermal treatment (nanocubes) or via dissolution and reentrant recrystallization processes (octahedra and cuboctahedra).



1. INTRODUCTION

A major advantage of the well-faceted (euhedral) nanocrystal catalytic materials over traditional heterogeneous catalysts of ill-defined shapes and broad distribution of particle sizes arises from their favorable structural and morphological uniformity.¹ Such materials allow for unparalleled insight into the quantitative structure–reactivity relationships under more realistic pressure and temperature conditions, in contrast to macroscopic single crystals used in surface science studies.^{2,3} A comprehensive in-depth understanding of the nanocrystal growth with controlled shapes is then of vital importance to master the reproducible large-scale production of high-quality photo/electro/catalytic nanomaterials.

Numerous experimental investigations supported by computational modeling have established that the performance of an oxide catalyst for a given reaction can be considerably enhanced by controlling the dimension and morphology of the grains.^{4–7} Such studies are made possible owing to considerable progress in the development of aposite bottom-up synthetic methods,⁸ nanocrystal modeling,^{9–12} and recent advances in the imaging of nanoobjects by electron microscopy.^{13–15} The last allows retrieving the requisite structural and morphological information, depending on the size and particular features of the investigated specimens.^{16–19}

Cobalt spinel is one of the most explored oxides with a remarkable record of widespread applications.^{20–23} Depending on the type and location of the introduced cations, the physical and chemical properties of doped Co_3O_4 can be tuned over a wide range of compositions without altering the overall spinel crystallographic structure.^{24–26} With regard to the particular structure of the exposed planes with disparate concentrations of the active sites, another possibility of the photo/electro/catalytic reactivity regulation stems from the remarkable ability of Co_3O_4 for shape modification.^{4,27–29} Those features make nanostructured spinel catalysts very attractive benchmark systems to explore their unique redox properties and the resultant reactivity in relation to the size- and shape-induced effects.

Among the many available methods for the liquid-phase synthesis of nanospinel catalysts of uniform morphology, the hydrothermal method is one of the most expedient

Received: July 24, 2020

Revised: October 27, 2020

Published: November 11, 2020



approaches.^{30,31} When it is sensibly designed, it allows attaining clear-cut polyhedral nanocrystals with a low extent of agglomeration. For this purpose, various organic capping and shape-directing reagents are often used,³² which have to be carefully removed prior to any sensible studies of the obtained nanocrystals. Typically, calcination in oxygen or air at moderate temperatures is used for this purpose, but this process is often not easy to fully accomplish under mild conditions. Enhancement of the temperature to favor combustion of the organic part may lead to undesired sintering of nanocrystals and their contamination by the residual carbon deposit. Hence, it is essential to optimize simple preparation methods for synthesis of polyhedral spinel nanocrystals with the desired shape and size by the sole adjustment of the synthesis conditions, but without the use of any auxiliary organic agents or exogenous oxidants that may contaminate the final product.

There have been several works^{33–36} and review articles^{22,27} devoted to the hydrothermal synthesis of bare and doped cobalt spinels of predefined morphology. Yet, the mechanism of the consecutive transformations of the involved intermediate phases that appear in the course of the synthesis is not comprehensively understood. So far, the most common model of the topotactic (111) $\text{Co}_3\text{O}_4\parallel(001)$ $\text{Co}(\text{OH})_2$ transformation of cobalt hydroxide into cobalt spinel under thermal and hydrothermal conditions, valid only in an aerobic environment, has been based on structural similarities between both of these terminations, supported by an analysis of the corresponding electron diffraction patterns.^{37–39}

Detailed investigations into the growth process of nanocrystals and the parameters that govern the growth mechanism reveal an important role of the oriented attachment (OA) in the shape development.³ The oriented attachment of nanoparticles is associated with their coalescent growth, where the primary crystallites spontaneously stick together according to a common crystallographic orientation of the facets.⁴⁰ Such processes are often involved in the hydrothermal synthesis of nanomaterials, leading to the formation of sub-micrometer mesocrystals, which may next be transformed into bulk single crystals.^{41–44} Another important mechanism that is widely involved in oxide materials synthesis consists of a topotactic transformation of layered double hydroxide (LDH) precursors directly into the spinel phase.^{45,46} In such a phase transition the two crystalline materials, the hydroxide precursor and the spinel oxide, exhibit distinct crystallographic relationships, which have a strong influence on the morphology of the burgeoning material.

In the present work we investigate systematically the principal steps of the hydrothermal synthesis of Co_3O_4 nanocrystals with a well-controlled morphology, using cobalt nitrate and sodium hydroxide as the sole precursor reagents. Several complementary experimental techniques such as XRD, RS, IR, TEM, and SEM were applied to monitor the synthesis progress, leading to the development of euhedral spinel nanocrystals of the required shape. The proposed mechanistic model of cobalt spinel formation was supported by DFT shape modeling with application of the Wulff construction. Despite the widespread use of the cobalt nanospinel and its derivatives as electro/photo/catalysts, there have been only a few papers devoted explicitly to the hydrothermal synthesis of Co_3O_4 nanocrystals, and none of them have dealt with the elucidation of an intimate mechanism of the spinel phase formation and

shape perfection of the produced nanocrystals into euhedral bulk solids.

2. EXPERIMENTAL SECTION

2.1. Synthesis. The Co_3O_4 nanoparticles with controlled polyhedral shape were synthesized by a hydrothermal method. In the standard procedure, specific amounts of $\text{Co}(\text{NO}_3)_2\cdot 6\text{H}_2\text{O}$ and NaOH precursor compounds, with a constant Co^{2+} to OH^- ratio equal to 2.7, were dissolved in 18 mL of demineralized water. The obtained mixture was stirred for 5 min and then transferred into a 20 mL Teflon lined stainless steel reactor and heated at 180 °C for 0.5, 1, 3, 5, and 8 h to provide the intermediate and final products. The obtained black spinel precipitate was separated from the supernatant by centrifugation at 3000 rpm for 5 min and washed with distilled water. The washing procedure was repeated at least five times. Finally, the synthesized Co_3O_4 nanocrystals were dried at 60 °C overnight.

2.2. Characterization. X-ray patterns were recorded with a Bruker D8-advance diffractometer, using $\text{Cu K}\alpha$ radiation ($\lambda = 1.540598$ Å). The diffractograms were recorded in the range of $2\theta = 10$ – 70° with steps of $0.02^\circ/\text{s}$. Raman spectra were recorded in the range 100–900 cm^{-1} with 1 cm^{-1} resolution by means of a Renishaw InVia spectrometer, using the wavelength excitation of 785 nm and nine scans for each measurement. The infrared ATR spectra were registered by means of a Nicolet 6700 spectrometer with a liquid- N_2 -cooled MCT detector. The spectra were recorded in the wavenumber range of 550–3900 cm^{-1} with an accumulation of 64 scans. SEM imaging of the gold-coated spinel nanocrystals was carried out on a Tescan instrument at a 20 kV acceleration voltage. A more detailed analysis was performed by transmission electron microscopy (TEM), using an FEI Tecnai Osiris microscope equipped with an X-FEG Schottky field emitter (200 kV) and a high angle annular dark field (HAADF) detector. The samples deposited on lacey-carbon-coated copper grids were imaged using a beryllium double-tilt low-background holder.

2.3. TEM Image Simulations. The constructed structural models of $\text{Co}_3\text{O}_4\parallel\text{Co}^{2+}(\text{OH})_{2-x}(\text{NO}_3)_x$ (Figure 6i), $\text{Co}_3\text{O}_4\parallel\text{CoOOH}\parallel\text{Co}^{2+}(\text{NO}_3)(\text{OH})_3$ (Figure 7b₁), and Co_3O_4 nanocrystals (Figure 7c₁) were used for simulation of the corresponding TEM images: Figures 6j and 7b,c, respectively. Simulated images were calculated by means of the multislice method implemented in the QSTEM software.⁴⁷ The Poisson noise at the level of 4% of the total contrast was added to the simulated images, in order to approach the experimental conditions. A complete list of the simulation parameters is presented in Table S1 in the Supporting Information.

2.4. DFT Modeling. The quantum-chemical calculations were performed with the VASP code 5.4.4 (Vienna Ab initio Simulation Package),⁴⁸ which utilizes the PAW⁴⁹ method to reconstruct the all-electron wave function. Methfessel–Paxton smearing⁵⁰ with $\sigma = 0.1$ eV was used. The bulk lattice constant was calculated by fitting the E/V values to the Birch–Murnaghan equation of state.⁵¹ The following optimization criteria were used: 10^{-6} eV for the SCF, 10^{-3} eV/Å for the geometry optimization, and a basis set cutoff energy of 500 eV. The value of the Hubbard U parameter was selected to be 4.4 and 6.7, for Co^{I} and Co^{O} , respectively.^{52–54} The DFTsol methodology,^{55,56} implemented in the VASPsol code, was used for a description of the solvation effects.⁵⁷ The effective dielectric constant of water at $T = 180$ °C and $p = 15$ bar was set to $\epsilon = 39.1$.⁵⁸

3. RESULTS AND DISCUSSION

3.1. Morphology of Co_3O_4 Nanocrystals: Influence of the Synthesis Conditions. In order to keep the minimum number of reactants for the synthesis of the Co_3O_4 nanocrystals (NCs), we selected cobalt nitrate and sodium hydroxide as the sole precursors. In both cases the residual counterions (NO_3^- and OH^-), possibly retained on the spinel surface, can be easily eliminated by calcination even under mild conditions, without leaving any persistent remains. Such precursors have been used previously for the synthesis of

Table 1. Synthesis Conditions Leading to Cubic, Cuboctahedral, and Octahedral Shapes of Cobalt Spinel Nanocrystals^a

morphology	$c_{\text{Co}^{2+}}$ (mol dm ⁻³)	c_{OH^-} (mol dm ⁻³)	$c_{\text{Co}^{2+}}/c_{\text{OH}^-}$	$\Delta c_{\text{Co}^{2+}}$ (mol dm ⁻³)
cubic	1.31	0.49	2.7	1.07
cuboctahedral	2.69	1.00	2.7	2.19
octahedral	4.09	1.52	2.7	3.33

^a $c_{\text{Co}^{2+}}$ and c_{OH^-} indicate the initial concentrations of cobalt nitrate and sodium hydroxide, respectively, whereas $\Delta c_{\text{Co}^{2+}}$ stands for change in the $\text{Co}^{2+}_{\text{aq}}$ concentration in the mother liquor after precipitation of the parent cobalt hydroxide.

cobalt spinel nanocubes by the precipitation method and subsequent aging at $\sim 100^\circ\text{C}$ under reflux under aerobic conditions.⁵⁹ A similar protocol of the cobalt spinel hydrothermal synthesis has also been used elsewhere;^{32,36} however, the principal mechanistic steps of the intricate pathways of Co_3O_4 formation and growth have not been comprehensively revealed and clarified. Herein, we demonstrate that by variation of only the concentrations of the $\text{Co}(\text{NO}_3)_2$ and NaOH reactants, while the $\text{Co}^{2+}/\text{OH}^-$ ratio is kept constant, it is possible to obtain spinel nanocrystals of various well-defined polyhedral morphologies under hydrothermal treatment at 180°C under anoxic conditions. In preliminary experiments we tested various $c_{\text{Co}^{2+}}/c_{\text{OH}^-}$ ratios, ranging from 2.7 to 3, 3.5, 4, and 4.5, and found that for the subsequent mechanistic studies $c_{\text{Co}^{2+}}/c_{\text{OH}^-} = 2.7$ is the most appropriate.

In Table 1 different compositions of the synthesis mixtures are shown, which lead to particular morphologies of the cobalt spinel nanocrystals, revealed by SEM imaging (Figure 1).

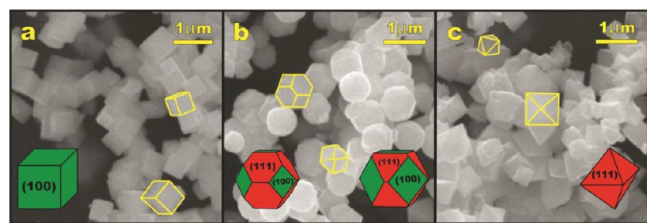


Figure 1. Polyhedral morphology of the cobalt spinel nanocrystals obtained under different hydrothermal synthesis conditions, (a) cubic shape obtained at $c_{\text{Co}^{2+}} = 1.31 \text{ mol dm}^{-3}$; (b) cuboctahedral at $c_{\text{Co}^{2+}} = 2.69 \text{ mol dm}^{-3}$; (c) octahedral shape at $c_{\text{Co}^{2+}} = 4.09 \text{ mol dm}^{-3}$. In all syntheses, a constant $c_{\text{Co}^{2+}}/c_{\text{OH}^-}$ ratio equal to 2.7 was maintained.

Generally, all of the examined spinel NCs exhibit well-developed polyhedral shapes with an apparent high flatness of the exposed surfaces. SEM observations of several distinct nanocrystals at different tilt angles allow for the preliminary assignment of the exhibited shapes to the most fitted polyhedral benchmark (see below).

As it is illustrated in Figure 1a, the average particle diameter of the cubic (hexahedral) nanocrystals enclosed by the six $\{100\}$ planes is equal to $d_{\text{cube}} = 780 \pm 60 \text{ nm}$ (gauged by the body diagonal). The 14-faceted polyhedral particles terminated by 8 $\{111\}$ and 6 $\{100\}$ planes are slightly larger, $d_{\text{cub-oct}} = 830 \pm 100 \text{ nm}$. Upon a move to nanocrystals of octahedral morphology exhibiting only the 8 $\{111\}$ planes and an average diameter of $d_{\text{octa}} = 820 \pm 100 \text{ nm}$, the particle size distribution becomes somewhat broader.

The accurate shapes of the observed 14-faceted polyhedra can be assessed using the (100)-(110)-(111) morphodrome of the $Fm\bar{3}m$ spinel NCs, reported elsewhere.⁶⁰ The shapes enclosed by the two types of planes, (100) and (111), with the abundance ratio of $R_{(111)/(100)}$, give rise to a truncated hexahedron for $0 < R < 1/2$, a cuboctahedron for $R = 1/2$,

and a truncated octahedron for $1/2 < R < 1$. Thus, the obtained nanocrystals, with $0.42 < R < 0.64$, can be assigned to specific nearly cuboctahedral to truncated octahedral morphologies (Figure 1). For the sake of conciseness they will jointly be called hereafter as a cuboctahedral shape, although in contrast to spinel cubes and octahedra their faceting is not as well developed and the corners still remain quite rounded. All nanocrystals of cobalt spinel are rather uniform in the size with a low degree of agglomeration, providing excellent model materials for sensible structure–activity investigations. The specific surface areas of the three kinds of Co_3O_4 NCs was measured by the Brunauer–Emmett–Teller (BET) method. The obtained values for Co_3O_4 cubes, cuboctahedra, and octahedra are equal to 2.26, 1.97, and $1.90 \text{ m}^2 \text{ g}^{-1}$, respectively.

The obtained results indicate that the actual morphology of the Co_3O_4 nanocrystals depends primarily on the amount of the $\text{Co}(\text{NO}_3)_2$ and NaOH precursors used in the synthesis, and not just on their molar ratio as has been suggested previously.^{36,59} As already mentioned, the latter quantity was kept constant at $[\text{Co}(\text{NO}_3)_2]/[\text{NaOH}] = 2.7$, with a purposeful stoichiometric excess of the cobalt cations with respect to the hydroxyl groups (see Table 1). The $\text{Co}^{2+}_{\text{aq}}$ and NO_3^- ions left in the mother liquor after precipitation of the precursor $\beta\text{-Co}(\text{OH})_2$ phase play an important role in its subsequent transformation into cobalt spinel under anoxic conditions (see below). For a low amount of the reactants, at a cobalt nitrate concentration of 1.31 mol dm^{-3} , the cobalt spinel nanocrystals are produced in the form of well-cut cubes (Figure 1a). When the amount of $\text{Co}(\text{NO}_3)_2$ (and accordingly NaOH) was enhanced to reach 2.69 mol dm^{-3} , the shape of the Co_3O_4 changed into a cuboctahedron (Figure 1b). With a further increase in the amount of cobalt nitrate to 4.09 mol dm^{-3} , the obtained spinel nanocrystals show an octahedral habit (Figure 1c). In all cases the initial pH of the reaction mixture was in the range of 6.2–6.5, the reaction temperature was $T = 180^\circ\text{C}$, and the overall pressure was $p = 15 \text{ bar}$.

In order to clarify the mechanism of the Co_3O_4 nanocrystal formation, and to unravel the chemical background for the observed phenomena, we examined the evolution of the phase composition and morphology of all the identified intermediate species by means of TEM, XRD, IR, and RS techniques at various time intervals. The initial green $\alpha\text{-Co}(\text{OH})_2$, precipitated upon mixing of the reactants, was spontaneously transformed into a more stable pink $\beta\text{-Co}(\text{OH})_2$, identified by the characteristic XRD diffraction pattern (JCPDS card #30-443). The results collated in Figure 2 show that, upon 1 h of the hydrothermal reaction, crystalline submicrometric sheets of the $\beta\text{-Co}(\text{OH})_2$ phase, present exclusively at the beginning of the reaction, are still dominant (Figure 2a₁). The position along with narrow shape of the (001) and other diffraction lines imply the formation of the well crystalline $\beta\text{-Co}(\text{OH})_2$ plates with a regular interlayer registry. Yet, multiple bands in the range $1000\text{--}1500 \text{ cm}^{-1}$ observed in the IR spectra (Figure 2a₂), apart from the O–H vibrations at 3642 cm^{-1} and Co–

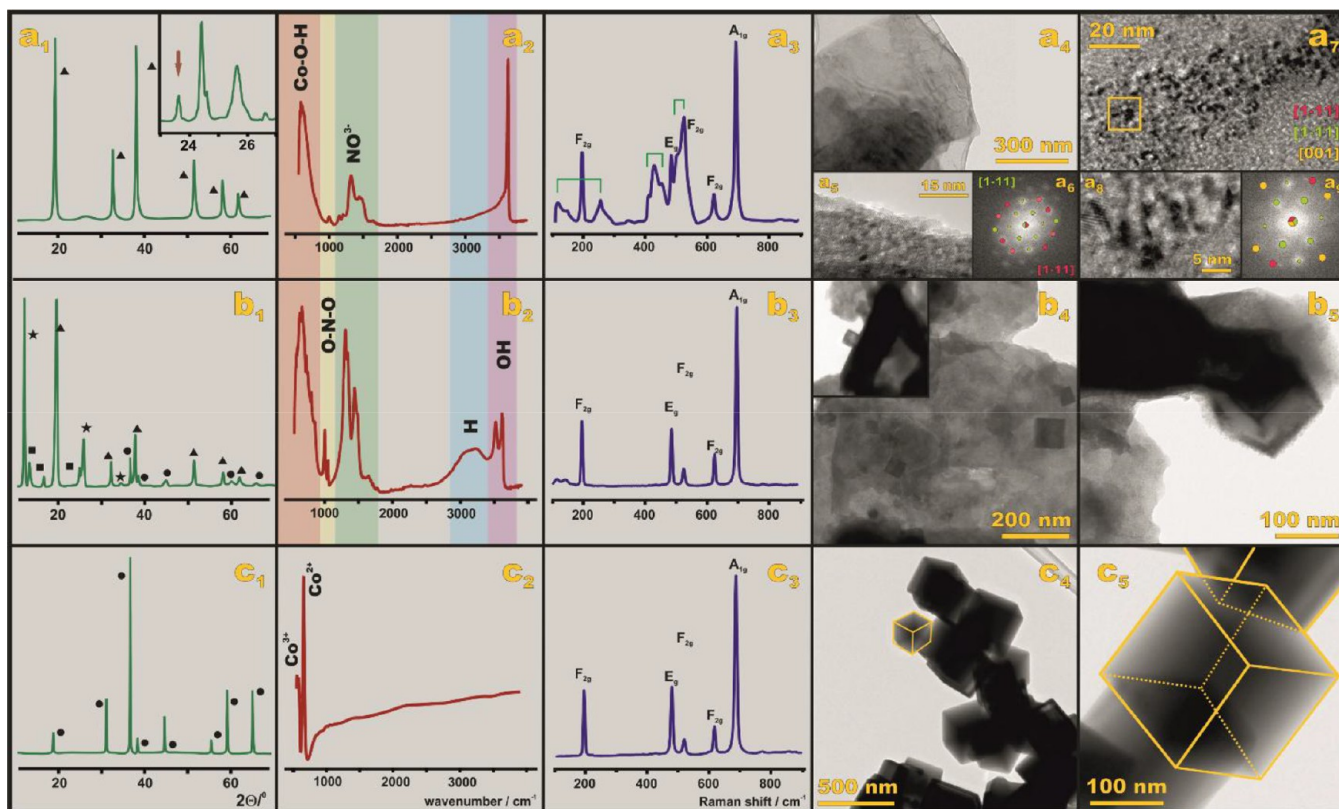
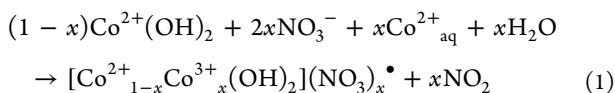
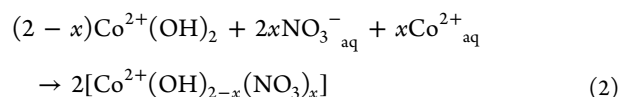


Figure 2. Synthesis stages of cubic cobalt spinel nanocrystals. XRD, IR, RS, and TEM data collected after 1 h (a₁–a₉, respectively), 5 h (b₁–b₅, respectively) and 8 h (c₁–c₅, respectively) of the hydrothermal reaction. The FFT patterns shown in the a₆ and a₉ inserts correspond to β -Co(OH)₂ (pink dots), Co₂(OH)₃NO₃ (green dots) and Co₃O₄ (yellow dots), respectively. The Raman bands of β -Co(OH)₂ and Co₃O₄ are labeled according to their symmetry species (a₃, b₃, c₃), whereas the cobalt hydroxide features are marked with brackets. The XRD patterns are assigned to β -Co(OH)₂ (▲), Co(NO₃)(OH)·H₂O (■), Co₂(NO₃)(OH)₃ (★), and Co₃O₄ (●) phases. For the sake of clarity, enlarged XRD, RS, and IR spectra are also reproduced in Figures S1–S7 in the Supporting Information.

OH at 628 cm^{−1} due to β -Co(OH)₂,⁶¹ reveal the presence of NO₃[−] anions ($\nu_2 = 1322$ cm^{−1}, $\nu_4 = 1442$ cm^{−1}, $\nu_1 = 1045$ cm^{−1}) of the local C_{2v} symmetry, associated with the cobalt centers.^{62–64} The band at 1632 cm^{−1} is characteristic for the $\delta_{\text{H-O-H}}$ vibrations of water molecules. Its presence is consistent with an appreciable bathochromic tailing of the intense and narrow peak at 3642 cm^{−1}, attributed to the stretching mode of the hydroxyl groups in the brucite-like layers, implying that some scarce water admolecules may be present in the interlayer gallery or on the external surface. These results indicate that on the surface and within the interlayer space of cobalt hydroxide some nitrate anions are trapped, according to the following reaction



leading to the appearance of a transient layered double hydroxide (LDH) phase.⁶³ This process is particularly favored just upon precipitation of cobalt hydroxide, when it is still in its incipient α -Co(OH)₂ polymorph with an expanded interlayer space. Since a residual dissolved oxygen is probably acting here as an oxidant, this phase is of minor abundance. A main pathway of the nitrate capture can occur in a nonredox fashion, via an anion exchange in the brucite-type layers when the framework hydroxyls are replaced by the nitrate anions



bringing about a steady development of cobalt hydroxide nitrates, which at the next stages of the hydrothermal reaction are seen in XRD quite clearly. Both reactions are made possible due to the presence of the abundant residual cobalt and nitrate ions in the solution, left upon the precipitation of Co(OH)₂ (Table 1). The LDH entities containing NO₃[−] are expected to exhibit larger interlayer spacings,⁶³ yet their distinction by XRD in the case of the simultaneous presence of other cobalt hydroxide nitrate phases is difficult because many diffraction lines are overlapping. However, upon inspection of the narrow region, recorded in the range $2\theta = 15$ – 30° after 2 h of the reaction, the appearance of the $[\text{Co}^{2+}_{1-x}\text{Co}^{3+}_x(\text{OH})_2](\text{NO}_3)_x$ species with the outer-sphere NO₃[−] was inferred from the clearly resolved discrete diagnostic peak at $2\theta = 23.53^\circ$, along with the akin Co(OH)(NO₃[−]) and Co₂(OH)₃(NO₃[−]) phases, containing nitrate anions in the first coordination sphere and the divalent cobalt alone (Figure 2a₁ insert). It is probably worth noting here that the latter phase can be formulated alternatively as Co(OH)_{3/2}(NO₃[−])_{1/2}, with a fourth of the OH[−] groups in the brucite-like layer replaced by the NO₃[−] anions.

More detailed information about the phase composition of this aliquot sample was obtained from Raman spectra shown in Figure 2a₃, where in addition to the bands at 255 (E_g), 429

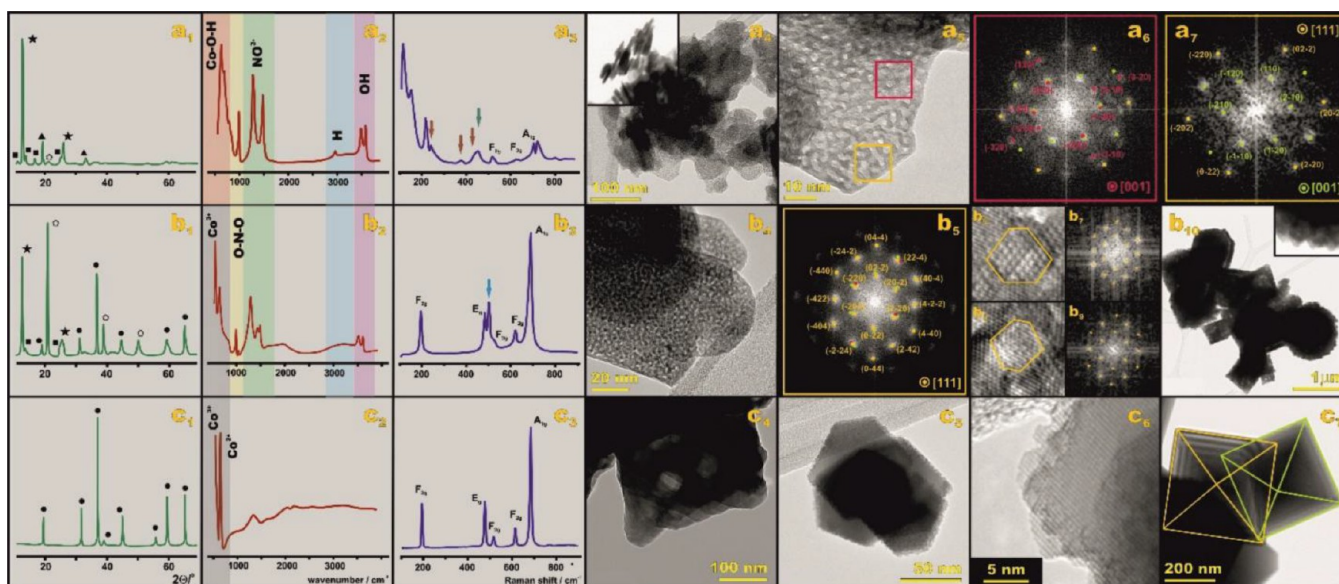


Figure 3. Main stages of the synthesis of octahedral cobalt spinel nanocrystals. XRD, IR, RS, and TEM data collected after 1/2 h (a_1 – a_7), 1 h (b_1 – b_{10}) and 5 h (c_1 – c_7) of the hydrothermal reaction. The XRD patterns are assigned to β -Co(OH) $_2$ (\blacktriangle), Co(NO $_3$)(OH)·H $_2$ O (\blacksquare), Co $_2$ (NO $_3$)(OH) $_3$ (\star), CoOOH (\diamond), and Co $_3$ O $_4$ (\bullet) phases. The FFT diffraction patterns (a_6) and (a_7) correspond to the regions marked by pink and yellow squares (a_5), respectively. They confirm the coexistence of the Co $_2$ (NO $_3$)(OH) $_3$ (a_6 , pink dots), CoOOH (a_6 , a_7 , green dots), and Co $_3$ O $_4$ (a_6 , a_7 , yellow dots) phases. Electron diffraction patterns (b_5 , b_7 , b_9), corresponding to the regions b_4 , b_6 (yellow hexagon), and b_8 (yellow hexagon), respectively, reveal the presence of the Co $_3$ O $_4$ phase alone. For the sake of clarity enlarged XRD, RS, and IR spectra are also reproduced in Figures S8–S19 in the Supporting Information.

(A_{1g}), and 507 cm^{-1} (A_{2u}), and the bands at 146, 280, 457, and 523 cm^{-1} assigned to β -Co(OH) $_2$,⁶⁵ apparent RS features characteristic of the nascent cobalt spinel grains (appearing at 194 cm^{-1} (F_{2g}), 484 cm^{-1} (E_g), 622 cm^{-1} (F_{2g}), and 693 cm^{-1} (A_{1g})) may already be distinguished.⁶⁶ Indeed, in the TEM pictures (Figure 2a $_4$ –a $_9$), apart from the large sub-micrometer β -Co(OH) $_2$ plates (Figure 2a $_4$ –a $_5$), the nature of which is confirmed by the FFT diffraction pattern (Figure 2a $_6$, pink dots), one may distinguish the presence of the Co $_2$ (OH) $_3$ NO $_3$ phase (Figure 2a $_6$, green dots) together with small (2–3 nm) blunt-shaped nascent cobalt spinel grains, nucleating from the parent platelike matrix (Figure 2a $_7$ –a $_8$). As the concentration of the precursor salt (nutrient) was the lowest among the examined samples (see Table 1), a lesser oversaturation caused by the hydrothermal decrease of the dielectric constant of the solvent (from $\epsilon \approx 80$ to $\epsilon \approx 40$) favors the generation of a smaller number of the crystallization nuclei than in the case of the octahedra synthesis, where the nutrient concentration was the highest (see below). The emerging Co $_3$ O $_4$ nuclei are separated from each other as well (Figure 2a $_8$). The FFT diffraction pattern shown in the inset definitely confirms their spinel structure (Figure 2a $_9$).

An analysis of the spectroscopic data of the specimens examined after 5 h of the hydrothermal synthesis reveals progress in the evolution of the phase composition of the reaction mixture. In the XRD pattern, except for the reflections due to the starting β -Co(OH) $_2$, characteristic lines due to Co(NO $_3$)(OH)·H $_2$ O, Co $_2$ (NO $_3$)(OH) $_3$, and Co $_3$ O $_4$ (JCPDS card #43-1003) are clearly visible. Accordingly, the multiple IR bands of the coordinated nitrate species (999, 1050, 1306, 1338, 1440, and 1482 cm^{-1}) increase considerably in relative intensity, and the OH bands around 3500–3600 cm^{-1} consequently decrease. The OH stretching band is now split into three distinct lines situated at 3626, 3614, and 3523 cm^{-1} (reflecting the coexistence of the hydroxide and hydroxide

nitrate phases, respectively), which are accompanied by a broad band centered at 3200 cm^{-1} . The latter is characteristic of hydrogen bond formation, implying the presence of some trapped water molecules in the case of the cobalt hydroxide nitrate phases with a more open interlayer space. The coordination of nitrates by the cobalt cations is nicely documented by development of the sizable IR peak at 1050 cm^{-1} associated with the $\nu_1(A_1)$ vibration, which is forbidden in the planar D_{3h} symmetry, and the concomitant splitting of the doubly degenerate $\nu_3(E')$ vibration into $\nu_2(A_1)$ and $\nu_4(B_2)$ bands upon lowering of the symmetry to C_{2v} . Their subsequent doubling into 1306, 1338 cm^{-1} and 1440, 1482 cm^{-1} lines reflects speciation of the coordinated NO $_3^-$ due to the simultaneous presence of the Co $_2$ (NO $_3$)(OH) $_3$ (alias Co(OH) $_{3/2}$ (NO $_3$) $_{1/2}$) and Co(NO $_3$)(OH)·H $_2$ O phases. Such features are consistent with gradual transformation of the cobalt hydroxide into the corresponding hydroxide nitrates and then into cobalt spinel (see the characteristic RS spectrum of Co $_3$ O $_4$ in Figure 2b $_3$).

At this stage of the reaction the initially blunt Co $_3$ O $_4$ grains become faceted upon growth (to release the strain accumulation), and the resultant spinel nanocubes of various nanometer sizes (10–70 nm) can be distinguished in the TEM pictures (Figure 2b $_4$ top view and side view in the inset). An analysis of the TEM image obtained at higher magnification discloses some intimate details of the Co $_3$ O $_4$ nanocrystal classic growth stage via incorporation of the precipitated adparticles on the surface (Figure 2b $_5$). The samples examined after 8 h of the synthesis time show the sole presence of well-shaped and uniform size cobalt spinel nanocrystals, as can be inferred from the concerted diagnostic XRD, IR, and RS spectra (Figure 2c $_1$ –c $_3$). Their cubic shape is nicely revealed by the TEM observations (Figure 2c $_4$). Closer inspection of a selected spinel grain at higher magnification (Figure 2c $_5$) confirms its euhedral, free of defects quality. Subsequent examination of the

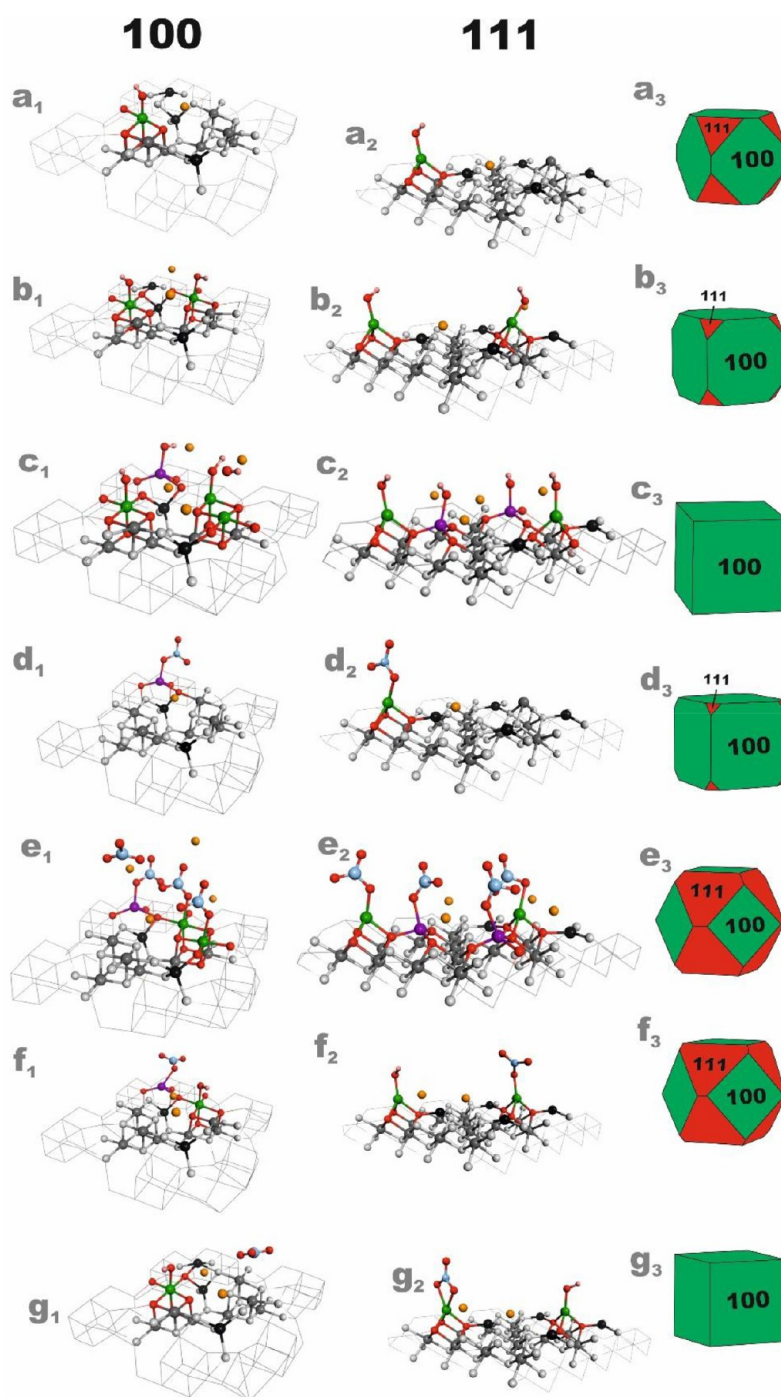


Figure 4. Lateral view of the (100) and (111) terminations of cobalt spinel, covered with OH^- (a), 2OH^- (b), 4OH^- (c), NO_3^- (d), 4NO_3^- (e), $\text{OH}^-/\text{NO}_3^-$ in configuration 1 (f), and $\text{OH}^-/\text{NO}_3^-$ species in configuration 2 (g), along with the corresponding equilibrium shapes of the Co_3O_4 nanocrystals predicted by means of Wulff construction using the values reported in Table 2. The orange balls represent the default Na^+ counterions. A more detailed version of this picture is given in Figures S20–S22 in the Supporting Information.

Co_3O_4 nanocubes separated from the solution by the TG/MS analysis revealed a small loss of the sample mass ($\Delta m \approx 0.035$ mg, 0.61%), associated with removal of the residual surface hydroxyl and nitrate adspecies.

Analogous physicochemical investigations were performed for the synthesis of the octahedral Co_3O_4 nanocrystals, and the results are collated in Figure 3.

Inspection of the data collated in Figure 3 shows that, in comparison to the synthesis of the spinel cubes, all stages of the reaction are now substantially accelerated. In the XRD

pattern of the sample examined after a few minutes upon mixing of the reactants, a combination of $\text{Co}_2(\text{NO}_3)(\text{OH})_3$, $\text{Co}(\text{NO}_3)(\text{OH})\cdot\text{H}_2\text{O}$, and CoOOH (JCPDS card #01-073-1213) phases along with the parent $\beta\text{-Co}(\text{OH})_2$ phase were found. The first phase becomes dominant after 30 min of the hydrothermal treatment (Figure 3a₁). The IR and RS spectra (Figure 3a₂, a₃) are consistent with the XRD results, yet the appearance of the distinct F_{2g} and A_{1g} Raman peaks characteristic of cobalt spinel indicates that at this stage some incipient Co_3O_4 grains were already formed. The

Table 2. Surface Energies of the (100) and (111) Terminations of Cobalt Spinel Covered by Various Amounts of OH[−] and NO₃[−], with Na⁺ Acting as the Counterion^a

coverage	γ_{100} (J m ^{−2}) (Δ%)	(100) surface abundance (%)	γ_{111} (J m ^{−2}) (Δ%)	(111) surface abundance (%)
bare surface	1.27 (0)		1.70 (0)	
OH [−]	1.09 (14)	77	1.37 (19)	23
2OH [−]	0.95 (25)	95	1.41 (17)	5
3OH [−]	0.74 (42)	99	1.22 (28)	1
4OH [−]	0.43 (66)	100	1.04 (39)	0
5OH [−]		100	1.22 (28)	0
6OH [−]		100	0.99 (42)	0
NO ₃ [−]	0.91 (28)	98	1.44 (15)	2
2NO ₃ [−]	0.93 (27)	98	1.48 (13)	2
4NO ₃ [−]	1.28 (−1)	46	1.33 (22)	54
5NO ₃ [−]		67	1.50 (12)	33
OH [−] /NO ₃ [−] (conf 1)	1.12 (12)	69	1.85 (−9)	31
OH [−] /NO ₃ [−] (conf 2)	0.39 (69)	98	1.40 (18)	2

^aΔ% defines changes in the surface energies in comparison to the γ values for the bare surfaces.

corresponding TEM pictures reveal the morphology of the sub-micrometer plate-shaped particles (Figure 3a₄,a₅), which are decorated by the embedded small (3–5 nm) Co₃O₄ crystallites. The FFT diffraction patterns (Figure 3a₆,a₇), taken from the regions marked by pink and yellow squares shown in Figure 3a₅, justify the simultaneous presence of the Co₂(NO₃)(OH)₃ (pink dots), CoOOH (green dots), and Co₃O₄ (yellow dots) phases in the interior of the plates (Figure 3a₆), whereas at the edge of the examined plate, the CoOOH phase with some Co₃O₄ contribution dominates (Figure 3a₇).

The changes in the phase composition of the reaction mixture after 1 h of the synthesis progress are shown in Figure 3b₁–b₃. The XRD pattern is now governed by the Co₂(NO₃)(OH)₃ and CoOOH reflections with a clearly enhanced Co₃O₄ contribution. Accordingly, the intensity of the nitrate multiplet in the IR spectrum decreases significantly (Figure 3b₂), whereas in the RS spectrum only the Co₃O₄ bands are visible (Figure 3b₃), illustrating nicely the lucid complementarity of the both vibrational spectroscopies for probing different aspects of the phase heterogeneity of such complex materials. The plates of the coexisting Co₂(NO₃)(OH)₃/CoOOH phases are around 100 nm in diameter (Figure 3b₄) and are densely intergrown with the preponderant small spinel crystallites (see below), the diagnostic FFT diffraction pattern of which is shown in Figure 3b₅. The magnified fragments of the TEM pictures and the corresponding FFT patterns (Figure 3b₆,b₇ and Figure 3b₈,b₉) reveal the polyhedral (most commonly truncated octahedral) shape of these primary Co₃O₄ nanocrystals with dimensions of 3–5 nm. The obtained results imply that during the hydrothermal treatment an important fraction of the Co²⁺ ions associated with the nitrate ligands was endogenously oxidized into Co³⁺ species for the successful formation of Co²⁺[Co³⁺₂O₄] entities out of the initially precipitated β -Co²⁺(OH)₂ phase, despite the anoxic conditions. The resultant primary spinel nanocrystallites tend to aggregate spontaneously into sub-micrometer mesocrystals of cobalt spinel with an apparent subhedral shape and a markedly rough external surface (see Figure 3b₁₀ and the inset). A more detailed inspection of the corresponding TEM images reveals that the large (~0.1–0.5 μ m) subhedral spinel grains are composed of much smaller congested truncated octahedra (5–50 nm), which are nucleated and grow out of the CoOOH and Co₂(NO₃)(OH)₃ phases. Due to a much higher concentration

of the nutrient (in comparison to the cubes), the enhanced supersaturation of the nutrient solution promotes a higher nucleation rate, giving rise to the appearance of a much larger amount of the prime cobalt spinel nanocrystals. Their subsequent growth and coalescence lead to an immediate crowding and the formation of a fairly dense texture of the resultant sub-micrometer grains, seen in Figure 3b₆,b₈. This process is favored by an enhanced ionic strength of the solution, which facilitates the nanocrystal agglomeration by attenuating the interparticle repulsion. Examination of the XRD, IR, RS, and TEM results recorded after 5 h (Figure 3c₁–c₇) shows definitively the sole presence of the Co₃O₄ nanocrystals of a sub-micrometer size. Figure 3c₄ illustrates spontaneous smoothing of the initially coarse surface (cf. Figure 3b₁₀), whereas spinel nanocrystals of transient subhedral and eventual octahedral shapes found in the batch are shown in Figure 3c₅,c₆ (magnified fragment) and Figure 3c₇, respectively. An IR feature below 1500 cm^{−1} indicates that some nitrate adspecies are still present on the surface of the obtained spinel octahedral nanocrystals (Figure 3c₂). Indeed, in comparison to the nanocubes, in the case of the octahedral crystallites the TG/MS analysis showed a larger weight loss of $\Delta m \approx 0.094$ mg (1.81%), due to removal of the residual surface NO₃[−] and OH[−] species, which is caused by the stronger attachment of those anions to the (111) termination than to the (100) plane (see Table S2 in the Supporting Information).

The obtained results document clearly that polyhedral, low-agglomeration spinel nanocrystals of a uniform size and controlled shape can be obtained from the sole cobalt nitrate and sodium hydroxide precursors by a mere variation of their concentration, while the concentration ratio and the reaction temperature are kept constant. The synthesized spinel nanocrystals are shown by XRD and RS to be free of the contaminant spurious phases; therefore, in contrast to the spinel NCs obtained previously from the same precursors,⁵⁹ subsequent purification in HCl, recommended therein, is not needed.

3.2. DFT Surface Energy Calculations and Shape Modeling. Molecular modeling of surface energies in conjunction with the Wulff construction allowed us to predict the equilibrium shape of the primary Co₃O₄ nanoparticles under the investigated hydrothermal conditions, also providing a suitable background to explain the observed morphological

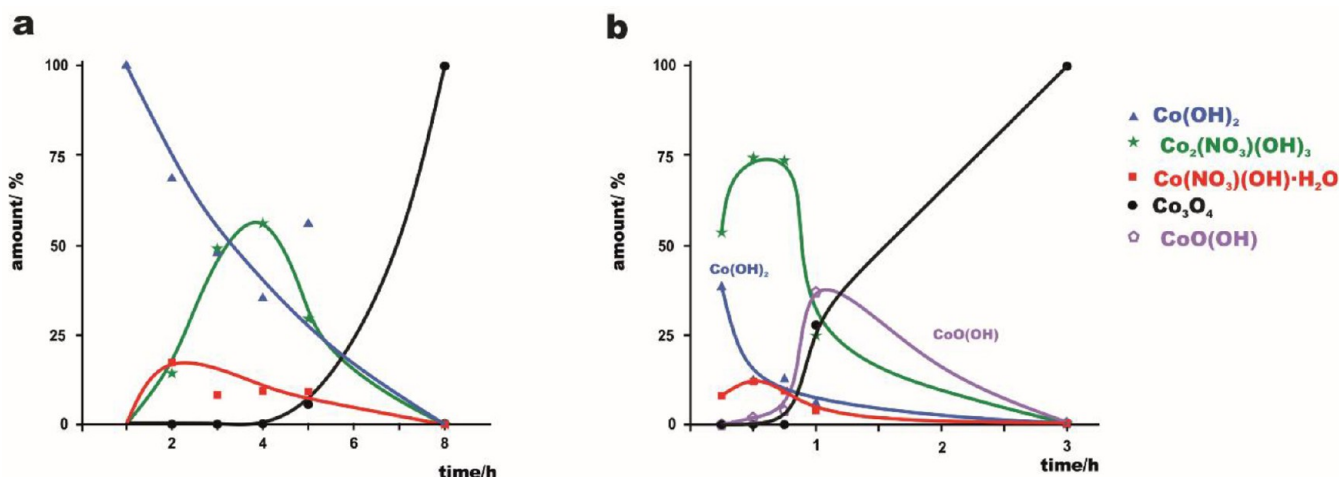


Figure 5. Successive phase transformations derived from the XRD measurements collated in Figures S25 and S26, leading to the formation of cobalt spinel nanocubes (a) and nano-octahedra (b).

changes. We calculated the surface energies of the key (100), (111), and (110) terminations covered by hydroxyls, nitrates, and mixed $\text{OH}^-/\text{NO}_3^-$ species, using Na^+ left in the mother liquor as a default counterion. Because in all of the examined surface coverage scenarios the appearance of the (110) facet was scarce and was always much smaller than the two other facets, for the sake of simplicity this termination was excluded from further consideration. The optimized structures of the exposed facets covered with representative combinations of the OH^- and NO_3^- adspecies are collected in Figure 4, whereas all other examined attachment modes (adsorption configurations) are shown in Figures S23 and S24, respectively, in the Supporting Information.

An inspection of Figure 4 shows that hydroxyl species are bound in a terminal fashion on both surfaces. The nitrates on the (100) facet are attached in a monodentate way, whereas they are attached on the (111) termination in mono- and bidentate forms with the O atom acting as a donor center. Adsorption energies of all the examined adsorption configurations of the OH^- and NO_3^- adspecies are collated in Table S2 in the Supporting Information. For the OH^- and NO_3^- anions there are substantial differences in the adsorption energies between the (100) and (111) facets, revealing a strong preference of the $\text{OH}^-/\text{NO}_3^-$ species for attachment to the (111) plane, especially at low coverages. As the amount of the surface-trapped anions increases, the adsorption energy decreases, and this effect is of particular importance for the (100) plane. The corresponding values of the surface energies, γ_{hkl} , for both terminations are collected in Table 2.

From a quick inspection of the results it is clear that, generally, the stabilization effect of the hydroxyls is smaller than that of the nitrate anions for the (100) facet, whereas for the (111) plane this difference is evidently attenuated. In all cases the covered (111) facet exhibits distinctly higher surface energies in comparison to the (100) termination. This effect is most pronounced for the planes containing mixed $\text{OH}^-/\text{NO}_3^-$ adspecies in configuration 2. The highest coverages by the hydroxyls correspond to four (three species attached to the surface, one OH^- group stabilized by the solvation cavity) and six OH^- groups for the (100) and (111) planes, respectively (Table S2 in the Supporting Information). In the case of nitrates the corresponding maximum coverage reaches four (100) (three species attached to the surface, one NO_3^- group

stabilized by the solvation cavity) and five (111) (four species attached to the surface, one NO_3^- group stabilized by the solvation cavity) NO_3^- anions. The mixed $\text{OH}^-/\text{NO}_3^-$ configurations are distinctly more stable than the $2\text{OH}^-/2\text{NO}_3^-$ configurations.

The calculated γ_{100} and γ_{111} values for various surface coverages can next be used in conjunction with the Wulff construction to reveal the equilibrium morphology of the corresponding spinel nanocrystals. The resultant polyhedra expose the prime (100) and (111) facets at various abundances (Figure 4), depending on the actual surface coverage. The attachment of OH^- enhances the development of the (100) termination, and the truncated cubes are predicted for the surface covered by one, two, and three OH^- groups. Above the coverage by three hydroxyls, the equilibrium shape of Co_3O_4 is thoroughly cubic (Figure 4c₃). The adsorbed nitrates show an opposite tendency, with enhancement of the number of the adsorbed NO_3^- anions. The initially nearly cubic morphology, dominant at the coverage by one or two nitrate molecules, evolves into a cuboctahedral shape when the coverage is above three molecules per the surface unit cell (Figure 4e₃). In the case of mixed ligands configuration 1 gives rise to cuboctahedral nanocrystals, whereas in configuration 2 a cubic shape is preferred (Figure 4f_{3,g}₃, respectively).

Generally, the results show a strong thermodynamic tendency toward cube or truncated cube morphologies of the primary cobalt spinel nanocrystals. The shapes close to the completely octahedral shape were never predicted in the examined conditions. Surface coverage by the NO_3^- anions seems to be favorable for the synthesis of cuboctahedral nanocrystals, whereas enhanced surface hydroxylation apparently favors cubes. The predicted shapes were taken as the reference morphologies for mechanistic considerations of the Co_3O_4 nanocrystal formation and faceting. It should be noted, however, that the final morphology of the synthesized spinels is also a matter of mechanistic and space confinement factors, which are addressed below in more detail by mechanistic considerations.

3.3. Mechanistic Pathways of Spinel Morphogenesis and Development of Specific Faceting. An analysis of the results collated in Figures 2 and 3 revealed that the cubic and octahedral nanocrystals were clearly produced along different routes and at different rates. Whereas the progress of the

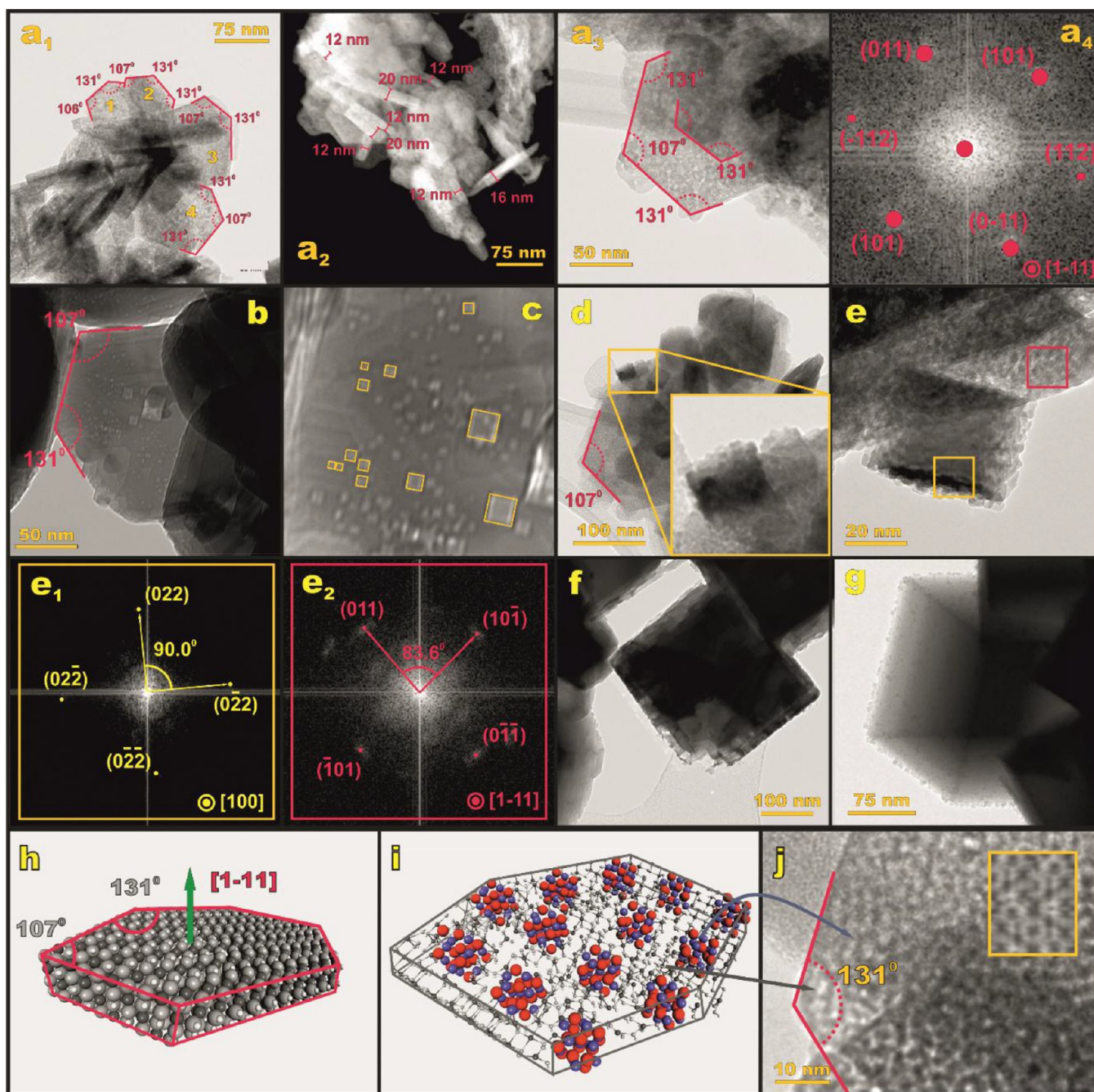
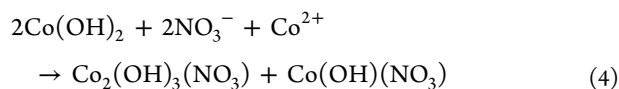
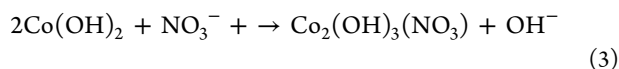


Figure 6. TEM pictures documenting topotactic transformation of the parent reactive $\text{Co}^{2+}(\text{OH})_{2-x}(\text{NO}_3)_x$ template into Co_3O_4 cubes. The PRT plates with the (1–11) basal planes (a_1), top view (a_2) and side view (a_3) and a selected plate viewed along the [1–11] direction and the corresponding FFT pattern (a_4). Random nucleation of spinel phase and coalescence of the grains (b , c), formation of meso-crystalline cubes via oriented attachment of the nanosized cuboidal building blocks (d , e) and FFT patterns of the regions marked by yellow and red squares revealing the [100]||[1–11] topotactic relationship between the Co_3O_4 crystals and the $\text{Co}^{2+}(\text{OH})_{2-x}(\text{NO}_3)_x$ template (e_1 , e_2), a sub-micrometer Co_3O_4 cubic crystal with a malformed edge due to an uncompleted process of the surface wrapping (f), and a single crystal of cobalt spinel decorated by precipitated entities during its growth via 2D attachment mechanism (g). An atomistic model of the $\text{Co}^{2+}(\text{OH})_{2-x}(\text{NO}_3)_x$ plate (h), the $\text{Co}^{2+}(\text{OH})_{2-x}(\text{NO}_3)_x$ template with the nucleating spinel phase (i), and the corresponding TEM image (j) with the simulated fragment delineated by a yellow rectangle (insert).

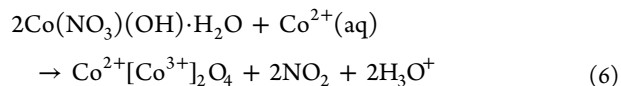
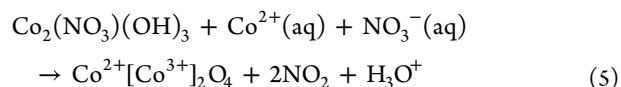
octahedral NC formation is rather prompt (the synthesis is fully accomplished within 3 h), in the case of the cubes it is distinctly more sluggish and takes 8 h to be completed (see also a full sequence of the collated XRD, IR, and RS spectra measured during the reaction progress in Figures S25 and S26). The spinel phase in the XRD-detectable amounts appears after 4 and 0.5 h of the reaction, respectively. The

proper sequential arrangement of the identified starting, intermediate, and final phases (Figure 5) and an analysis of the evolution of the grain morphologies allowed the discovery of a pronounced difference in the formation and growth mechanisms of the specifically faceted cobalt spinel nanocrystals.

In the case of the cube-shaped nanocrystals during the hydrothermal treatment, in contact with the residual $\text{Co}(\text{NO}_3)_2$ solution (see Table 1), the starting $\beta\text{-Co}(\text{OH})_2$ phase (blue curve) is gradually transferred in parallel into the dominant $\text{Co}_2(\text{NO}_3)(\text{OH})_3$ (green) and lesser $\text{Co}(\text{NO}_3)(\text{OH})\cdot\text{H}_2\text{O}$ (red) intermediate phases



They exhibit relative content maxima at about 2–3 and 3–4 h of the reaction progress, respectively (Figure 5a). Apparently the process of $\text{OH}^-/\text{NO}_3^-$ ligand exchange (eqs 3 and 4) is more likely to occur than the alternative much more reluctant oxidative intercalation of the $\beta\text{-Co}(\text{OH})_2$ matrix by the nitrate anions. The latter would lead to the formation of the layered double hydroxide $[\text{Co}^{2+}_{1-x}\text{Co}^{3+}_x(\text{OH})_2](\text{NO}_3^-)_x$ phase and requires the presence of an exogenous oxidant such as O_2 (or H_2O_2 , which is also used quite often⁶⁷). As already mentioned, in order to reach the cobalt spinel stoichiometry, an appropriate fraction of the Co^{2+} cations must be oxidized into the Co^{3+} species. However, the estimated total amount of dioxygen dissolved in the reaction mixture and present in the gas phase of the tightly closed autoclave ($V = 20$ mL with 80% of filling), assessed as $\sim 4 \times 10^{-5}$ M, was 2 orders of magnitude lower than the amount of oxygen required to accomplish the required cobalt oxidation ($\sim 2 \times 10^{-3}$ M). This residual dissolved oxygen is most likely responsible for the appearance of the minor $[\text{Co}^{2+}_{1-x}\text{Co}^{3+}_x(\text{OH})_2](\text{NO}_3^-)_x$ species; as a result the main course of the hydrothermal synthesis takes place in a practically anoxic environment. Thus, at this stage of the reaction a vast majority of the cobalt ions preserve their initial divalent state. This implies that the abundant nitrates present in the mother liquor after the precipitation of $\beta\text{-Co}(\text{OH})_2$, which are incorporated next to produce the hydroxyl nitrate intermediate phases, have to play the role of an actual cobalt oxidant.⁶⁸ The overall redox process $\text{Co}^{2+} + \text{NO}_3^- \rightarrow \text{Co}^{2+}-(\text{O}-\text{NO}_2)^- \rightarrow \text{Co}^{3+}-\text{O}^{2-} + \text{NO}_2$ is thought to produce the required trivalent Co^{3+} cations along with the O^{2-} anions needed to reach the final $\text{Co}^{2+}:\text{Co}^{3+}:\text{O}^{2-}$ stoichiometry out of the divalent cobalt hydroxide, during the hydrothermal oxidation reaction. The requisite attachment of the NO_3^- species to the cobalt cations was directly confirmed by the IR spectra, in particular by the observed band $\nu_1 = 1050$ cm^{-1} that is characteristic of NO_3^- bound to the cobalt centers and is forbidden in the D_{3h} symmetry of the planar freestanding anion. The sharp peak at 1380 cm^{-1} , diagnostic for the flat $D_{3h}\text{-NO}_3^-$ anions located in the interlayer space,⁶⁹ is lacking in the IR spectra in Figures 2 and 3, accordingly. Further hydrothermal treatment leads to an inner-sphere metal to ligand electron transfer within the $\text{Co}^{2+}-(\text{O}-\text{NO}_2)^-$ unit and detachment of the resultant neutral NO_2 moiety. The presence of a brown NO_2 gas in the autoclave after the reaction (detected organoleptically at first) was definitely confirmed by means of QMS spectroscopy. In the case of $\text{Co}_2(\text{NO}_3)(\text{OH})_3$ and $\text{Co}(\text{NO}_3)(\text{OH})\cdot\text{H}_2\text{O}$ by invoking the dissolved Co^{2+} cations and NO_3^- anions left in the mother liquor upon the $\text{Co}(\text{OH})_2$ precipitation (see Table 1), we may propose the following overall reactions to take place:



For the sake of conciseness, a $\text{Co}^{2+}(\text{OH})_{2-x}(\text{NO}_3)_x$ formulation is used hereafter (when needed) for designation of both distinct $\text{Co}_2(\text{OH})_3(\text{NO}_3)$ and $\text{Co}(\text{OH})(\text{NO}_3)$ phases detected during the reaction course, with $x = 1/2, 1$, respectively, as they jointly constitute a parent reactive template (PRT) for spinel phase formation. In accordance with these reaction schemes, the acidity of the solution decreased from the initial value of pH 6.5 to pH 2.1 due to the release of the hydronium ions. Such processes may occur in a rather gross fashion concurrently with the prerequisite Co^{2+} oxidation to Co^{3+} , since formation of a distinct Co^{3+}OOH phase was not observed in this case (Figure 5a). Nonetheless, an analogous reaction can also be envisioned to proceed in restricted areas for the cobalt hydroxyl nitrate entities with insufficient NO_3^- ligands ($x < 1/2$ on average), already at the early stages of the reaction as a minor pathway. Indeed, once the critical $\text{Co}^{2+}:\text{Co}^{3+}:\text{O}^{2-}$ ratio of at least an imperfect spinel stoichiometry is achieved locally, random nucleation and subsequent growth of the nascent Co_3O_4 crystals are made possible, as revealed in Figure 2a₂. Apparently, oxidation of Co^{2+} to Co^{3+} provides an intrinsic incentive for the nucleation of nascent spinel kernels. The nitrate anions trapped from the solution along with the dissolved $\text{Co}^{2+}(\text{aq})$ cations are gradually consumed with the progressing development of the spinel phase, and an equivalent amount of the protons is released. As is discussed below, the autogenously produced nitric acid plays an important role in hydrothermal etching of the produced spinel in its immature meso-crystal state.

A more in depth insight into the structural aspects of the proposed mechanism of the spinel formation can be inferred from an analysis of the series of TEM images collated in Figure 6. The key mechanistic indication here is provided by the presence of the hydrothermally produced elongated hexagonal $\text{Co}^{2+}(\text{OH})_{2-x}(\text{NO}_3)_x$ plates exhibiting the (1–11) basal plane (Figure 6a₁). The shape of these plates is features the characteristic angles of 131 and 107° observed typically in TEM images (Figure 6a₁–a₃), along the diffraction spots of clearly uneven intensities (Figure 6a₄), corresponding to the (1–11) basal plane. Such plates have been observed previously,⁷⁰ and they should be not misidentified with the often reported akin regular hexagonal $\beta\text{-Co}(\text{OH})_2$ crystallites. The latter exhibit the (001) basal plane,^{71,72} and feature all angles equal to 120°, together with even intensities of all the diffraction spots (see Figure S27 in the Supporting Information). The thickness of the cobalt hydroxyl nitrate plates varies from 12 to 20 nm (Figure 6a₂), indicating that they are composed of 15–25 sheets.

The indexed FFT pattern shown in Figure 6a₄ unequivocally validates the [1–11] orientation of these plates. The TEM image presented in Figure 6b eventually confirms that the spinel nucleation occurs randomly within the $\text{Co}^{2+}(\text{OH})_{2-x}(\text{NO}_3)_x$ template and that the appearing nano-sized cuboidal Co_3O_4 crystallites exhibit a nearly common vertical orientation imposed by the topotactic features of this process. An example of the resultant alignment of the spinel grains along the common [100] director is shown in Figure 6c.

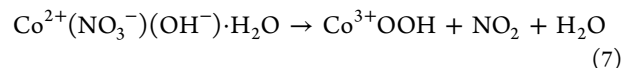
Formation of the separated Co_3O_4 domains in Figure 6b,c is in line with the conjecture that the layered reactive template \rightarrow spinel transformation takes place according to spontaneous nucleation and growth processes with the vital participation of the dissolved cobalt nitrate and is extended in time. Apparently, the nucleation rate is sensitive to fluctuations in the concentration of the $\text{Co}(\text{NO}_3)_2$ nutrient in the mother liquor. The emerging Co_3O_4 domains grow further at the expense of the PRT matrix and/or via coalescence. Once the substrate of the reactive template becomes virtually devoured, subsequent mesoscale self-assembly of the produced primary 2–3 nm crystallites to larger aggregates leads to the formation of approximately rectangular meso-crystals of ~ 50 – 100 nm size (Figure 6d,e). Since the spinel domains are produced from a single $\text{Co}^{2+}(\text{OH})_{2-x}(\text{NO}_3)_x$ plate, the ensuing Co_3O_4 crystallites inherit the common crystallographic orientation of the parent template due to the $[100]\text{Co}_3\text{O}_4\parallel[1-11]\text{-Co}^{2+}(\text{OH})_{2-x}(\text{NO}_3)_x$ topotactic relationship, as implied by the FFT patterns for the regions marked by the red and yellow squares (Figure 6e₁,e₂). The structural compatibility of both the square (100) and (1–11) frameworks (see Figure S28a in the Supporting Information) facilitates the topotactic character of this transformation. It probably explains also why the resultant primary Co_3O_4 nanocuboids can maintain the initial thickness of the precursor plates and thereby a uniform size to large extent. Since the preliminarily spinel cuboids have similar native dimensions, their consecutive merging via imperfect oriented attachment into spinel mesocrystals of a sub-micrometer size is greatly facilitated (Figure 6d–f).

The TEM image presented in Figure 6f shows some nuances of the late stage of the sub-micrometer spinel cube growth, where at one of the corners some building blocks are apparently still missing. The final compact (euhedral) submicron cubes of cobalt spinel are shown in Figure 6g. The visible fine entities decorating the surface are characteristic of the residual classic 2D surface growth mechanism,⁷³ which proceeds until an equilibrium with the surrounding solution is reached. As a result, the Co_3O_4 cubic nanocrystals are produced via the nutrient-mediated topotactic nucleation and crystallization with their $[100]$ directions inheriting the $[1-11]$ direction of the $\text{Co}^{2+}(\text{OH})_{2-x}(\text{NO}_3)_x$ PRT plates. An atomistic model of the parent hexagonal hydroxyl nitrate platelet and the incipient spinel domains nucleated out of this template are shown in Figure 6h,i. It should be noted, however, that the number density of the cobalt atoms in Co_3O_4 ($\sim 45 \text{ nm}^{-3}$) is almost 2 times higher than in the parent $\text{Co}^{2+}(\text{OH})_{2-x}(\text{NO}_3)_x$ template phase ($\sim 24 \text{ nm}^{-3}$). Such a volumetric misfit gives rise to local disorder in the intergrain region and even to partial disruption of the PRT plates, while the spinel framework integrity is maintained. At an extreme, it may also lead to the appearance of hollow patches, observed for example upon vigorous thermal decomposition of $\beta\text{-Co}(\text{OH})_2$ under aerobic conditions, reported previously.⁷⁴

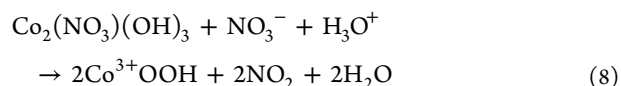
The diffusionless topotactic transformation is mainly engaging the Co cations within the brucite-like sheets that are oxidized and relocated in the new spinel 16d positions. It also entails incorporation of the O^{2-} anions produced upon NO_3^- decomposition along with the capture of the solvent $\text{Co}^{2+}(\text{aq})$ cations (at 8a sites) required to build up the ultimate spinel lattice. The volumetric disparity of both frameworks leads to considerable structural disorder in the interfacial region, which is nicely revealed by the corresponding TEM picture, interpreted quantitatively by the image simulation

(Figure 6j), using the model shown in Figure 6i. The experimental image fits quite well the simulated TEM picture (insert), speaking in favor of the presence of disordered interfacial zones around the nascent spinel grains. As a result, the intimate mechanism of the $\text{Co}^{2+}(\text{OH})_{2-x}(\text{NO}_3)_x \rightarrow \text{Co}_3\text{O}_4$ conversion can be treated as a topotactic process mediated by the dissolved cobalt nitrate, contributing in concert to the spinel framework formation. The proposed scenario is an alternative account to the surface-wrapping mechanism of spinel cube formation, suggested previously elsewhere.⁵⁹ The resultant 5–10 nm primary cubic nanocrystals (Figure 6c), being arranged in a certain crystallographic registry in the course of hydrothermal treatment, are assembled into larger Co_3O_4 mesocrystals (Figure 6d,e), following the imperfect oriented attachment mechanism.⁷⁵ In such sub-micrometer grains, still without coherent material linking the assembled building blocks, the precursor and solvent molecules may be located within the space between the aligned crystallites. They are next used as binding species in the hydrothermal recrystallization step, where the formed mesocrystals are gradually consolidated into the compact well-cut sub-micrometer cubes shown in Figure 6f,g. Prior formation of a mesocrystal, as a requisite midway step of the latter process, has been suggested previously.^{76,77}

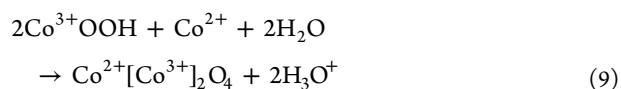
In the case of the hydrothermal synthesis with a high concentration of the nitrate precursor, the OH^- ligand exchange by nitrates in the precipitated $\beta\text{-Co}(\text{OH})_2$ layers is quick, and within 0.5 h the $\text{Co}_2(\text{NO}_3)(\text{OH})_3$ phase dominates the reaction mixture (Figure 5b). Subsequent oxidation of the divalent cobalt cations in the $\text{Co}^{2+}(\text{NO}_3^-)(\text{OH}^-)\cdot\text{H}_2\text{O}$ phase by the ligated NO_3^- anions leads to immediate (within 1 h) formation of the CoOOH precursor containing only Co^{3+} :



In parallel, CoOOH may also be formed at the expense of $\text{Co}_2(\text{NO}_3)(\text{OH})_3$ in a more involved reaction:



Then, the resultant Co^{3+}OOH , along with $\text{Co}^{2+}(\text{OH})_{2-x}(\text{NO}_3)_x$, can be converted readily into cobalt spinel with participation of the residual $\text{Co}^{2+}(\text{aq})$ cations, following the reaction



The resultant drop of the pH value to 3.7 is smaller than in the case of the spinel cubes synthesis (pH 2.1), as the formation of CoOOH is accompanied by consumption of protons (eq 8). As a result, owing to an abundance of nitrates, the cobalt oxidation and spinel nucleation processes become substantially accelerated. Indeed, the synthesis of the Co_3O_4 octahedra, which proceeds with concurrent involvement of the cobalt oxyhydroxide and hydroxyl nitrate phases, is shortened from 8 to 3 h in comparison to the cube synthesis (cf. Figure 5a,b).

Mechanistic details of the genesis of cobalt spinel octahedra can be deduced from analysis of the TEM data collated in Figures 3 and 7. Inspection of Figure 7a shows that the plates of the parent reactive template, in contrast to the spinel cube synthesis, exhibit a hexagonal shape with the edges subtending

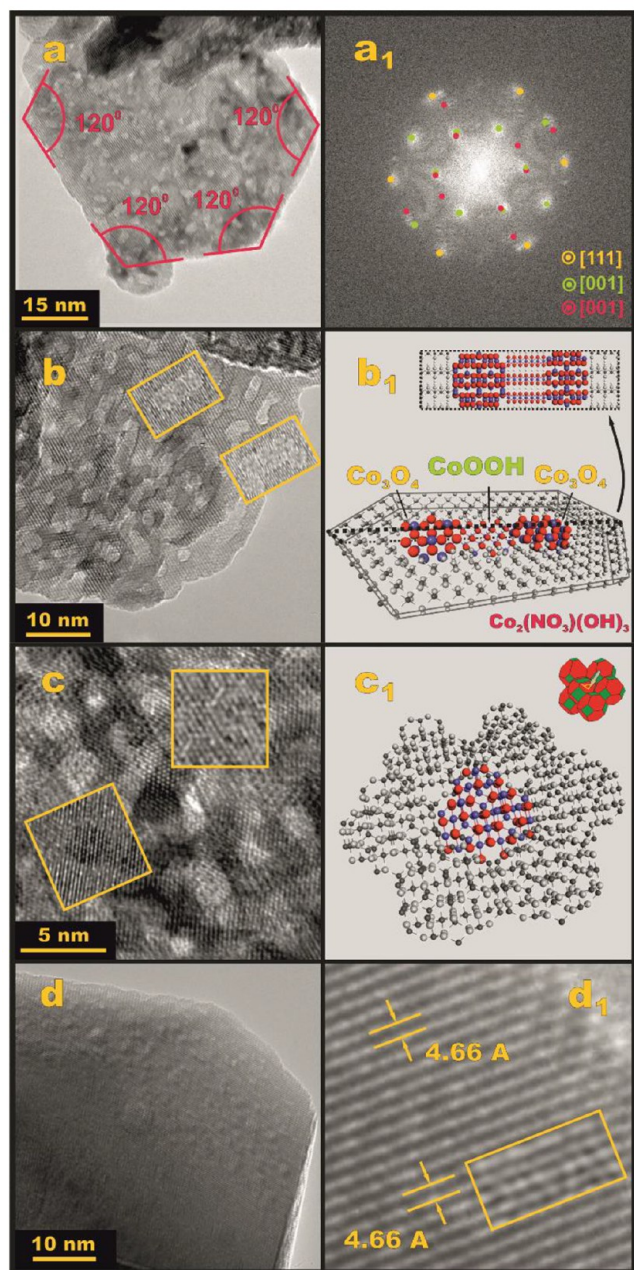


Figure 7. TEM pictures documenting topotactic transformation of the cobalt hydroxo nitrate template into the prime cuboctahedral Co_3O_4 crystallites. The parent $\text{Co}_2(\text{NO}_3)(\text{OH})_3$ plates that exhibit the (001) basal planes with the characteristic values of the interplanar angles of 120° (a) are oxidized into CoOOH and transformed topotactically into Co_3O_4 with the participation of the dissolved Co^{2+} and NO_3^- ions. The corresponding FFT pattern is shown in (a₁), where $\text{Co}_2(\text{NO}_3)(\text{OH})_3$ is marked by pink dots, CoOOH by green dots, and Co_3O_4 by yellow dots. The coexistence of CoOOH and Co_3O_4 truncated octahedral nanocrystals embedded in the parent $\text{Co}_2(\text{NO}_3)(\text{OH})_3$ matrix was confirmed by the inserted simulated fragments (b), using the atomistic model shown in (b₁). TEM image of the mosaic texture composed by the Co_3O_4 nanocrystals with the corresponding simulated regions (both inserts) and the corresponding atomistic model (c₁). TEM image of a consolidated Co_3O_4 nanocrystal (d), exhibiting the (111) termination with the inserted simulated fragment.

only the 120° angles. The corresponding FFT pattern shows that such plates are composed of a mixture of the

$\text{Co}_2(\text{NO}_3)(\text{OH})_3$, CoOOH , and nascent Co_3O_4 phases, which exhibit a $[111]\text{Co}_3\text{O}_4\parallel[001]\text{CoOOH}, \text{Co}_2(\text{NO}_3)(\text{OH})_3$ topotactic relationship. The latter favors formation of the (111) facets by the incipient spinel crystallites, facilitated by the topological compatibility of the hexagonal (111) and (001) frameworks (see Figure S28b in the Supporting Information). As a result the Co_3O_4 crystallites are preferentially exposing the (111) facets (Figure 7b,b₁,c). An atomistic model of the nascent Co_3O_4 crystallites grown out of the $\text{Co}_2(\text{NO}_3)(\text{OH})_3/\text{CoOOH}$ template is shown in Figure 7b₁ and was used to simulate the TEM images (seen in the insets in Figure 7b), reproducing well the observed pattern of the lattice fringes and the characteristic contrast features resulting from the coexistence of the $\text{Co}_3\text{O}_4/\text{CoOOH}$ (lighter contrast) and $\text{Co}_2(\text{NO}_3)(\text{OH})_3$ (dark contrast) regions as well. With the progress of the reaction the spinel crystallites form a compact texture, stemming from the competition for space with the growing progress (Figure 7c). The observed changes in the image contrast result from a slight mutual disorientation of the spinel crystallites due to an imperfect attachment mechanism being involved. A model of such a texture, shown in Figure 7c₁, was used for the image simulation, satisfactorily imitating the essential traits of the observed TEM picture (Figure 7c with both simulated inserts). When the higher concentration of the nutrient left in the mother liquor (Table 1) and the adsorption energies reported in Table S2 are taken into account, the surface of the primary crystallites should be decorated mainly by NO_3^- adspecies. Such conditions are predicted to be thermodynamically favorable for the appearance of cuboctahedral crystallites (Figure 4e₁–e₃), nicely corroborating the experimental TEM observations and substantiating the model used for the image simulation as well (Figures 3b₆,b₈ and 7c,c₁).

At the late stage of the hydrothermal reaction, the congested spinel polycrystallites are finally transformed into a single crystal with the (111) plane primarily exposed (see Figure 7d,d₁ for the magnified fragment showing the interplanar distance of $d_{(111)} = 4.66 \text{ \AA}$ with the corresponding simulation). Successful annihilation of the intergrain boundaries in the hydrothermally consolidated bulk Co_3O_4 single crystal is clearly documented in Figure 7d, yet some remnant irregularities of the exposed surface, reflecting its implicated origin, are still visible.

The whole series of molecular, structural, and morphological events leading to the formation of the bulk euhedral Co_3O_4 nanocrystals of a given polyhedral shape is collated in Figure 8. It can be divided into three stages: parent reactive template (PRT) formation, nutrient-assisted topotactic nucleation (NTN), and nanocrystal morphogenesis (NCM). The sequence of the consecutive phase changes $\beta\text{-Co}(\text{OH})_2 \rightarrow \{[\text{Co}_2(\text{NO}_3)(\text{OH})_3, \text{Co}(\text{OH})_3(\text{NO}_3^-)\cdot\text{H}_2\text{O}, \text{Co}^{2+}_{1-x}\text{Co}^{3+}_x(\text{OH})_2](\text{NO}_3^-)\cdot n\text{H}_2\text{O}\} \rightarrow \text{CoOOH}$ leads to the development of the parent reactive template. The $\text{Co}^{2+}_{1-x}\text{Co}^{3+}_x(\text{OH})_2](\text{NO}_3^-)\cdot n\text{H}_2\text{O}$ species of the LDH structure play an important role in the presence of only an exogenous oxidant. Under the anoxic conditions LDH can appear as a merely spurious phase, since an endogenous oxidation of Co^{2+} to Co^{3+} mediated by the coordinated NO_3^- (produced in the prior $\text{OH}^-/\text{NO}_3^-$ ligand exchange step) plays the crucial role here (Figure 8, top left). The shape of the PRT plates, dictated by the concentration of the nutrient in the mother liquor, governs the nutrient-assisted topotactic nucleation of the spinel crystallites. The PRT plates produced at a low concentration

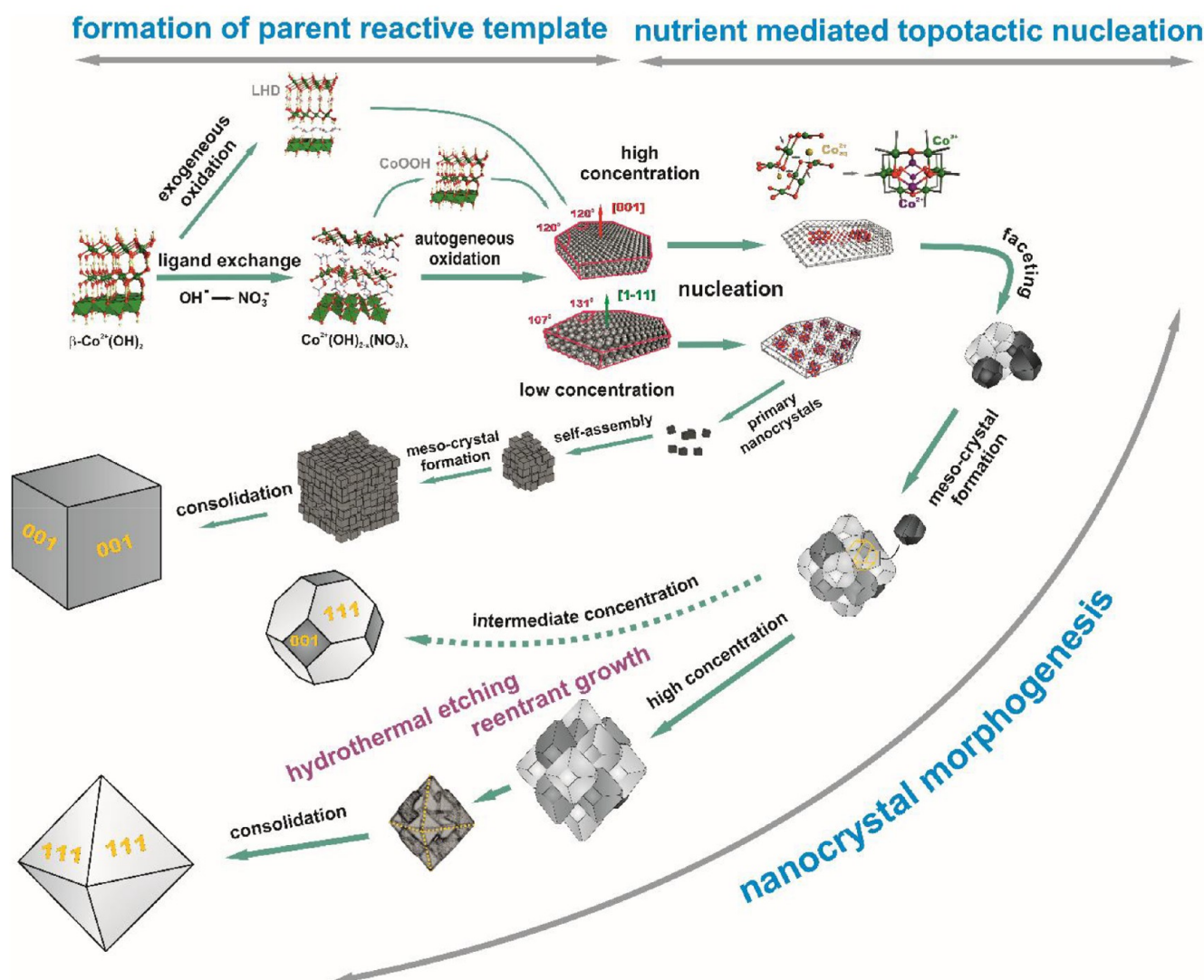


Figure 8. A series of structural and morphological changes leading to the development of cobalt spinel sub-micrometer crystals from the precipitated β -Co(OH) $_2$ under hydrothermal conditions. The principal stages of the reaction include the formation of the parent reactive template (top left), nutrient-assisted topotactic nucleation (top right), and nanocrystal morphogenesis (bottom), leading to the development of cubic (low concentration of nutrient), truncated octahedral (medium concentration), and octahedral shapes of Co $_3$ O $_4$ (high concentration). At the top of the NTN section the displacement of the cobalt cations during the topotactic transformation (in the directions indicated by green arrows), which give rise to the formation of a core atomic arrangement of the spinel framework, are shown.

of the nutrient exhibiting preferentially the (1–11) planes provide the template for the Co $_3$ O $_4$ nucleation in the form of cubes, whereas at higher concentrations the plates with the (001) basal plane (enriched in CoOOH) are involved in the topotactic nucleation of the truncated octahedra, in line with the DFT predictions. The required intimate displacements of the cobalt ions from the atomic positions occupied in the brucite-like layer and incorporation of the Co $^{2+}$ (aq) cations into 16d (Co $^{3+}$) and 8a (Co $^{2+}$) sites in the spinel framework are shown in Figure 8 (top right).

The primary nanocubes of Co $_3$ O $_4$ evolve from the nucleated 3–5 nm nanograins through subsequent growth and coalescence. In this stage, owing to their topotactic origin, they attain a fairly good crystallographic alignment, despite distinct spatial separation from one another. The primary Co $_3$ O $_4$ nanoparticles are next self-assembled to produce mesocrystals, and their fairly uniform cuboidal shape and size plays a beneficial role in this process (NCM stage), since

evenly sized building units are needed to develop the bulk cubic architecture over a wide size range. Subsequent hydrothermal recrystallization and framework consolidation gives rise to the formation of euhedral cubic Co $_3$ O $_4$ crystals of sub-micrometer dimensions. Due to the low concentration of the nutrient the whole process of the hydrothermal synthesis, slowed down particularly in the PRT and NCM stages where the NO $_3^-$ and Co $^{2+}$ (aq) species are explicitly involved, is rather sluggish (8 h).

In the case of the octahedral crystals, the course of the morphogenesis is distinctly different. Owing to the higher concentration of the nutrient a more vigorous nucleation gives rise to incipient agglomeration of the abundant nascent crystallites, which adopt a truncated-octahedral shape, also predicted by the DFT modeling. Their self-assembly leads to the formation of subhedral mesocrystals with a rough external surface. Yet, such a malformed morphology still exposes distinct facets, crinkled only by steps, kinks, and other

topologic irregularities. Since depletion of the nutrient stops the nucleation process, further shape evolution occurs via hydrothermal etching in the autogenously produced nitric acid, together with the re-entrant growth. After 3 h of reaction time, their joined action leads to spectacular surface flattening with preferential development of the (111) facets. Upon final hydrothermal consolidation of the crystal structure, clear-cut single-crystal octahedra are formed. At a medium concentration of the nutrient, the shape evolution ceases at the stage where both (111) and (100) planes are exposed, and the resultant spinel assumes an approximate cuboctahedral habit.

4. CONCLUSIONS

A detailed mechanism of the anoxic hydrothermal synthesis of euhedral Co_3O_4 nanocrystals with narrow size distribution, under a constant $c_{\text{Co}^{2+}}/c_{\text{OH}^-}$ ratio and varying concentration of the $\text{Co}(\text{NO}_3)_2$ and NaOH precursors, was established. At a nutrient concentration of 1.31 mol dm^{-3} regular cubic ($780 \pm 60 \text{ nm}$), at 2.69 mol dm^{-3} nearly cuboctahedral ($830 \pm 100 \text{ nm}$), and at 4.09 mol dm^{-3} octahedral ($820 \pm 100 \text{ nm}$) cobalt spinel nanocrystals are formed. The NO_3^- anions play the key roles of an oxidant, an oxygen donor, and, by controlling the surface energy, a shape-directing agent for the spinel formation. The shape of the nascent Co_3O_4 crystallites is primarily governed by the crystallographic constraints imposed by the nutrient-assisted in situ topotactic transformation. The spinel random nucleation occurs with the [100] or [111] direction of the Co_3O_4 facets inheriting the [1–11] direction (formation of cubes) or [001] direction (formation of octahedra) of the PRT plates. Sub-micrometer bulk cubic single crystals are produced via a mesocrystal stage, owing to an imperfectly oriented attachment of the primary cuboidal building nanoblocks. Bulk Co_3O_4 octahedra are formed by spontaneous self-assembly of the prime truncated octahedral nanocrystals into compact agglomerates of a malformed polyhedral shape. Surface smoothing and preferential development of the (111) termination occurs via hydrothermal etching and reentrant growth. High concentrations of the nutrient favor an octahedral shape, whereas a medium concentration favors a cuboctahedral shape.

This study also provides useful guidelines for a general synthetic approach to the rational hydrothermal production of other nanosized metal oxides, where not only the nature of the nutrient but also its concentration in the mother liquor play a decisive role.

■ ASSOCIATED CONTENT

Supporting Information

The Supporting Information is available free of charge at <https://pubs.acs.org/doi/10.1021/acs.cgd.0c01031>.

Parameters for TEM image simulation of models presented in Figure 6 and 7, adsorption energies of OH^- and NO_3^- species attached to (100) and (111) terminations of cobalt spinel facets, XRD data collected after 1 h of cubic cobalt spinel nanocrystal hydrothermal synthesis, XRD data collected after 2 h of cubic cobalt spinel nanocrystal hydrothermal synthesis, XRD data collected after 5 h of cubic cobalt spinel nanocrystal hydrothermal synthesis, XRD data collected after 8 h of cubic cobalt spinel nanocrystal hydrothermal synthesis, IR data collected after 1 h of cubic cobalt spinel nanocrystal hydrothermal synthesis, IR data collected

after 5 h of cubic cobalt spinel nanocrystal hydrothermal synthesis, IR data collected after 8 h of cubic cobalt spinel nanocrystal hydrothermal synthesis, Raman data collected after 1 h of cubic cobalt spinel nanocrystal hydrothermal synthesis, Raman data collected after 5 h of cubic cobalt spinel nanocrystal hydrothermal synthesis, Raman data collected after 8 h of cubic cobalt spinel nanocrystal hydrothermal synthesis, XRD data collected after 0.5 h of octahedral cobalt spinel nanocrystal hydrothermal synthesis, XRD data collected after 1 h of octahedral cobalt spinel nanocrystal hydrothermal synthesis, XRD data collected after 5 h of octahedral cobalt spinel nanocrystal hydrothermal synthesis, IR data collected after 0.5 h of octahedral cobalt spinel nanocrystal hydrothermal synthesis, IR data collected after 1 h of octahedral cobalt spinel nanocrystal hydrothermal synthesis, IR data collected after 5 h of octahedral cobalt spinel nanocrystal hydrothermal synthesis, Raman data collected after 0.5 h of octahedral cobalt spinel nanocrystal hydrothermal synthesis, Raman data collected after 1 h of octahedral cobalt spinel nanocrystal hydrothermal synthesis, Raman data collected after 5 h of octahedral cobalt spinel nanocrystal hydrothermal synthesis, lateral view of the (100) and (111) terminations of cobalt spinel covered with OH^- , 2OH^- , and 4OH^- , along with the corresponding equilibrium shapes of the Co_3O_4 nanocrystals predicted by means of Wulff construction using the values reported in Table 2, lateral view of the (100) and (111) terminations of cobalt spinel covered with NO_3^- and 4NO_3^- along with the corresponding equilibrium shapes of the Co_3O_4 nanocrystals predicted by means of Wulff construction using the values reported in Table 2, atomic structures of Na^+OH^- species adsorbed on (100) and (111) cobalt spinel facets, atomic structures of Na^+NO_3^- species adsorbed on (100) and (111) cobalt spinel facets, XRD, IR, and Raman spectra recorded in the course of the synthesis of Co_3O_4 cubes, XRD, IR, and Raman spectra recorded in the course of the synthesis of Co_3O_4 octahedra, simulated FFT patterns of $\beta\text{-Co}(\text{OH})_2$ plates oriented along (1–11) and (001) axes, and structural compatibility of the square (1–11) and (100) frameworks fostering the development of cubes and the (001) and (111) frameworks fostering the formation of the octahedral nuclei (PDF)

■ AUTHOR INFORMATION

Corresponding Authors

Joanna Gryboś – Faculty of Chemistry, Jagiellonian University, 30-387 Kraków, Poland; orcid.org/0000-0002-9777-0268; Email: grybosjo@chemia.uj.edu.pl

Zbigniew Sojka – Faculty of Chemistry, Jagiellonian University, 30-387 Kraków, Poland; Email: sojka@chemia.uj.edu.pl

Authors

Camilo Hudy – Faculty of Chemistry, Jagiellonian University, 30-387 Kraków, Poland

Angelika Gryczynska – Faculty of Chemistry, Jagiellonian University, 30-387 Kraków, Poland

Witold Piskorz – Faculty of Chemistry, Jagiellonian University, 30-387 Kraków, Poland; orcid.org/0000-0002-3462-436X

Complete contact information is available at:
<https://pubs.acs.org/10.1021/acs.cgd.0c01031>

Notes

The authors declare no competing financial interest.

ACKNOWLEDGMENTS

This work was supported by the Polish National Science Centre (NCN) Project OPUS-14, No 2017/27/B/ST4/01155. C.H. was partially supported by the Doctoral Project POWR.03.02.00-00-I004/16.

REFERENCES

- (1) Zhou, K.; Li, Y. Catalysis Based on Nanocrystals with Well-Defined Facets. *Angew. Chem., Int. Ed.* **2012**, *51*, 602–613.
- (2) Somorjai, G. A.; Park, J. Y. Molecular Factors of Catalytic Selectivity. *Angew. Chem., Int. Ed.* **2008**, *47*, 9212.
- (3) Dalmaschio, C. J.; Ribeiro, C.; Leite, E. R. Impact of the colloidal state on the oriented attachment growth mechanism. *Nanoscale* **2010**, *2*, 2336–2345.
- (4) Chizallet, C.; Costentin, G.; Lauron-Pernot, H.; Krafft, J.-M.; Che, M.; Delbecq, F.; Sautet, P. Assignment of photoluminescence spectra of MgO powders: TD-DFT cluster calculations combined to experiments. Part I: structure effects on dehydroxylated surfaces. *J. Phys. Chem. C* **2008**, *112*, 16629–16637.
- (5) Zasada, F.; Gryboś, J.; Budiyo, E.; Janas, J.; Sojka, Z. Oxygen species stabilized on the cobalt spinel nano-octahedra at various reaction conditions and their role in catalytic CO and CH₄ oxidation, N₂O decomposition and oxygen isotopic exchange. *J. Catal.* **2019**, *371*, 224–235.
- (6) Anke, S.; Bendt, G.; Sinev, I.; Hajiyani, H.; Antoni, H.; Zegkinoglou, I.; Jeon, H.; Pentcheva, R.; Roldan Cuenya, B.; Schulz, S.; Muhler, M. Selective 2-Propanol Oxidation over Unsupported Co₃O₄ Spinel Nanoparticles: Mechanistic Insights into Aerobic Oxidation of Alcohols. *ACS Catal.* **2019**, *9*, 5974–5985.
- (7) Trovarelli, A.; Llorca, J. Ceria Catalysts at Nanoscale: How Do Crystal Shape catalysis. *ACS Catal.* **2017**, *7*, 4716–4735.
- (8) Ghiasse, M.; Rezaei, M.; Meshkani, F.; Mobini, S. Preparation and optimization of the MnCo₂O₄ powders for low temperature CO oxidation using the Taguchi method of experimental design. *Res. Chem. Intermed.* **2019**, *45*, 4501–4515.
- (9) Barnard, A. S.; Curtiss, L. A. Computational Nano-morphology: Modeling Shape as well as Size. *Rev. Adv. Mater. Sci.* **2005**, *105*–109.
- (10) Barmparis, G. D.; Lodziana, Z.; Lopez, N.; Remediakis, I. N. Nanoparticle shapes by using Wulff constructions and first-principles calculations. *Beilstein J. Nanotechnol.* **2015**, *6*, 361–368.
- (11) Loschen, C.; Carrasco, J.; Neyman, K. M.; Illas, F. First-principles LDA+U and GGA+U Study of Cerium Oxides: Dependence on the Effective U Parameter. *Phys. Rev. B: Condens. Matter Mater. Phys.* **2007**, *75*, 35115.
- (12) Montoya, A.; Haynes, B. S. Periodic Density Functional Study of Co₃O₄ Surfaces. *Chem. Phys. Lett.* **2011**, *502*, 63–68.
- (13) Tan, J. P. Y.; Tan, H. R.; Boothroyd, Ch.; Foo, Y. L.; He, Ch. B.; Lin, M. Three-Dimensional Structure of CeO₂ Nanocrystals. *J. Phys. Chem. C* **2011**, *115*, 3544–3551.
- (14) Zasada, F.; Piskorz, W.; Stelmachowski, P.; Kotarba, A.; Paul, J.-F.; Płociński, T.; Kurzydłowski, K. J.; Sojka, Z. Periodic DFT and HR-STEM Studies of Surface Structure and Morphology of Cobalt Spinel Nanocrystals – Retrieving 3D Shapes from 2D Images. *J. Phys. Chem. C* **2011**, *115*, 6423–6432.
- (15) Crosby, L.; Enterkin, J.; Rabuffetti, F.; Poeppelmeier, K.; Marks, L. Wulff shape of strontium titanate nanocuboids. *Surf. Sci.* **2015**, *632*, L22–L25.
- (16) Wang, Z. L. Transmission Electron Microscopy of Shape-Controlled Nanocrystals and Their Assemblies. *J. Phys. Chem. B* **2000**, *104*, 1153–1175.
- (17) Ringe, E. Nanocrystalline Materials: Recent Advances in Crystallographic Characterization Techniques. *IUCr* **2014**, *1*, 530–539.
- (18) Xu, X.; Saghi, Z.; Gay, R.; Möbus, G. Reconstruction of 3D morphology of polyhedral nanoparticles. *Nanotechnology* **2007**, *18*, 225501–225509.
- (19) Su, D. Advanced electron microscopy characterization of nanomaterials for Catalysis. *Green Energy & Environment* **2017**, *2*, 70–83.
- (20) Zhao, Q.; Yan, Z.; Chen, C.; Chen, J. Spinel: Controlled Preparation, Oxygen Reduction/Evolution Reaction Application, and Beyond. *Chem. Rev.* **2017**, *117*, 10121–10211.
- (21) Liotta, L. F.; Wu, H.; Pantaleo, G.; Venezia, A. M. Co₃O₄ nanocrystals and Co₃O₄–MO_x binary oxides for CO, CH₄ and VOC oxidation at low temperatures: a review. *Catal. Sci. Technol.* **2013**, *3*, 3085–3102.
- (22) Xie, X.; Shen, W. Morphology control of cobalt oxide nanocrystals for promoting their catalytic performance. *Nanoscale* **2009**, *1*, 50–60.
- (23) Lukashuk, L.; Yigit, N.; Rameshan, R.; Kolar, E.; Teschner, D.; Hävecker, M.; Knop-Gericke, A.; Schlögl, R.; Föttinger, K.; Rupprechter, G. Operando Insights into CO Oxidation on Cobalt Oxide Catalysts by NAP-XPS, FTIR, and XRD. *ACS Catal.* **2018**, *8*, 8630–8641.
- (24) Hill, R. J.; Craig, J. R.; Gibbs, G. V. Systematics of the spinel structure type. *Phys. Chem. Miner.* **1979**, *4*, 317–339.
- (25) Liu, X.; Wang, H.; Lavina, B.; Tu, B.; Wang, W.; Fu, Z. Chemical Composition, Crystal Structure, and Their Relationships with the Intrinsic Properties of Spinel-Type Crystals Based on Bond Valences. *Inorg. Chem.* **2014**, *53*, 5986–5992.
- (26) Brik, M. G.; Suchocki, A.; Kamińska, A. Lattice Parameters and Stability of the Spinel Compounds in Relation to the Ionic Radii and Electronegativities of Constituting Chemical Elements. *Inorg. Chem.* **2014**, *53*, 5088–5099.
- (27) Sun, H.; Ang, H. M.; Tadé, M. O.; Wang, S. Co₃O₄ nanocrystals with predominantly exposed facets: synthesis, environmental and energy applications. *J. Mater. Chem. A* **2013**, *1*, 14427–14442.
- (28) Gasparotto, A.; Barreca, D.; Bekermann, D.; Devi, A.; Fischer, R. A.; Fornasiero, P.; Gombac, V.; Lebedev, O. I.; Maccato, C.; Montini, T.; Van Tendeloo, G.; Tondello, E. F-Doped Co₃O₄ Photocatalysts for Sustainable H₂ Generation from Water/Ethanol. *J. Am. Chem. Soc.* **2011**, *133*, 19362–19365.
- (29) Su, D.; Dou, S.; Wang, G. Single Crystalline Co₃O₄ Nanocrystals Exposed with Different Crystal Planes for Li-O₂ Batteries. *Sci. Rep.* **2015**, *4*, 1–9.
- (30) Kwon, J.; Kim, J.-H.; Kang, S.-H.; Choi, C.-J.; Rajesh, J. A.; Ahn, K.-S. Facile hydrothermal synthesis of cubic spinel AB₂O₄ type MnFe₂O₄ nanocrystallites and their electrochemical performance. *Appl. Surf. Sci.* **2017**, *413*, 83–91.
- (31) Reith, L.; Lienau, K.; Cook, D. S.; Moré, R.; Walton, R. I.; Patzke, G. R. Monitoring the Hydrothermal Growth of Cobalt Spinel Water Oxidation Catalysts: From Preparative History to Catalytic Activity. *Chem. - Eur. J.* **2018**, *24*, 18424–18435.
- (32) Huang, Z.; Zhao, Y.; Song, Y.; Li, Y.; Wu, G.; Tang, H.; Zhao, J. Study on the oxidation process of cobalt hydroxide to cobalt oxides at low temperatures. *RSC Adv.* **2016**, *6*, 80059–80064.
- (33) Xu, R.; Zeng, H. Ch. Control of Surface Area and Porosity of Co₃O₄ via Intercalation of Oxidative or Nonoxidative Anions in Hydrotalcite-like Precursors. *J. Phys. Chem. B* **2003**, *107*, 926–930.
- (34) Teng, Y.; Yamamoto, S.; Kusano, Y.; Azuma, M.; Shimakawa, Y. One-pot hydrothermal synthesis of uniformly cubic Co₃O₄ nanocrystals. *Mater. Lett.* **2010**, *64*, 239–242.
- (35) Yang, J.; Sasaki, T. Morphological Control of Single Crystalline Co₃O₄ Polyhedrons: Selective and Nonselective Growth of Crystal Planes Directed by Differently Charged Surfactants and Solvents. *Cryst. Growth Des.* **2010**, *10*, 1233–1236.
- (36) Xiao, X.; Liu, X.; Zhao, H.; Chen, D.; Liu, F.; Xiang, J.; Hu, Z.; Li, Y. Facile Shape Control of Co₃O₄ and the Effect of the Crystal

Plane on Electrochemical Performance. *Adv. Mater.* **2012**, *24*, 5762–5766.

(37) Tian, L.; Huang, K.; Liu, Y.; Liu, S. Topotactic synthesis of Co_3O_4 nanoboxes from $\text{Co}(\text{OH})_2$ nanoflakes. *J. Solid State Chem.* **2011**, *184*, 2961–2965.

(38) Kobayashi, Y.; Ke, X.; Hata, H.; Schiffer, P.; Mallouk, T. E. Soft Chemical Conversion of Layered Double Hydroxides to Superparamagnetic Spinel Platelets. *Chem. Mater.* **2008**, *20*, 2374–2381.

(39) Ortega, K. F.; Anke, S.; Salamon, S.; Ozcan, F.; Heese, J.; Andronesco, C.; Landers, J.; Wende, H.; Schuhmann, W.; Muhler, M.; Lunkenbein, T.; Behrens, M. Topotactic Synthesis of Porous Cobalt Ferrite Platelets from a Layered Double Hydroxide Precursor and Their Application in Oxidation Catalysis. *Chem. - Eur. J.* **2017**, *23*, 12443–12449.

(40) Sushko, M. L. Understanding the driving forces for crystal growth by oriented attachment through theory and simulations. *J. Mater. Res.* **2019**, *34*, 2914–2927.

(41) Niederberger, M.; Cölfen, H. Oriented attachment and mesocrystals: Non-classical crystallization mechanisms based on nanoparticle assembly. *Phys. Chem. Chem. Phys.* **2006**, *8*, 3271–3287.

(42) Penn, R. L.; Soltis, J. A. Characterizing crystal growth by oriented aggregation. *CrystEngComm* **2014**, *16*, 1409–1419.

(43) Boles, M. A.; Engel, M.; Talapin, D. V. Self-Assembly of Colloidal Nanocrystals: From Intricate Structures to Functional Materials. *Chem. Rev.* **2016**, *116*, 11220–11289.

(44) Lee, E. J. H.; Ribeiro, C.; Longo, E.; Leite, E. R. Oriented Attachment: An Effective Mechanism in the Formation of Anisotropic Nanocrystals. *J. Phys. Chem. B* **2005**, *109*, 20842–20846.

(45) Zhu, J.; Bai, L.; Sun, S. Y.; Zhang, X.; Li, Q.; Cao, B.; Yan, W.; Xie, Y. Topochemical transformation route to atomically thick Co_3O_4 nanosheets realizing enhanced lithium storage performance. *Nanoscale* **2013**, *5*, 5241–5246.

(46) Lou, X. W.; Deng, D.; Lee, J. Y.; Feng, J.; Archer, L. A. Self-Supported Formation of Needlelike Co_3O_4 Nanotubes and Their Application as Lithium-Ion Battery Electrodes. *Adv. Mater.* **2008**, *20*, 258–262.

(47) Koch, C.; *Determination of core structure periodicity and point defect density along dislocation*; Arizona State University: 2002.

(48) Kresse, G.; Furthmüller, J. Efficiency of ab-initio total energy calculations for metals and semiconductors using a plane-wave basis set. *Comput. Mater. Sci.* **1996**, *6*, 15–50.

(49) Blöchl, P. E. Projector augmented-wave method. *Phys. Rev. B: Condens. Matter Mater. Phys.* **1994**, *50*, 17953–17979.

(50) Methfessel, M.; Paxton, A. T. High-precision sampling for Brillouin-zone integration in metals. *Phys. Rev. B: Condens. Matter Mater. Phys.* **1989**, *40*, 3616–3621.

(51) Murnaghan, F. D. The Compressibility of Media under Extreme Pressures. *Proc. Natl. Acad. Sci. U. S. A.* **1944**, *30*, 244–247.

(52) Qiao, L.; Xiao, H. Y.; Meyer, H. M.; Sun, J. N.; Rouleau, C. M.; Puzos, A. A.; Geohegan, D. B.; Ivanov, I. N.; Yoon, M.; Weber, W. J.; Bieganski, M. D. Nature of the band gap and origin of the electrophoto-activity of Co_3O_4 . *J. Mater. Chem. C* **2013**, *1*, 4628–4641.

(53) Selcuk, S.; Selloni, A. DFT+U Study of the Surface Structure and Stability of Co_3O_4 (110): Dependence on U. *J. Phys. Chem. C* **2015**, *119*, 9973–9979.

(54) O'Brien, C. J.; Rák, Z.; Brenner, D. W. Free energies of $(\text{Co}, \text{Fe}, \text{Ni}, \text{Zn})\text{Fe}_2\text{O}_4$ spinels and oxides in water at high temperatures and pressure from density functional theory: Results for stoichiometric NiO and NiFe_2O_4 surfaces. *J. Phys.: Condens. Matter* **2013**, *25*, 445008.

(55) Fishman, M.; Zhuang, H. L.; Mathew, K.; Dirschka, W.; Hennig, R. G. Accuracy of exchange-correlation functionals and effect of solvation on the surface energy of copper. *Phys. Rev. B: Condens. Matter Mater. Phys.* **2013**, *87*, 245402.

(56) Mathew, K.; Sundararaman, R.; Letchworth-Weaver, K.; Aris, T. A.; Hennig, R. G. Implicit solvation model for density-functional study of nanocrystal surfaces and reaction pathways. *J. Chem. Phys.* **2014**, *140*, 084106.

(57) Letchworth-Weaver, K.; Arias, T. A. Joint density functional theory of the electrode-electrolyte interface: Application to fixed electrode potentials, interfacial capacitances, and potentials of zero charge. *Phys. Rev. B: Condens. Matter Mater. Phys.* **2012**, *86*, 75140.

(58) Uematsu, M.; Frank, E. U. Static Dielectric Constant of Water and Steam. *J. Phys. Chem. Ref. Data* **1980**, *9*, 1291–1306.

(59) Feng, J.; Zeng, H. Ch. Size-Controlled Growth of Co_3O_4 Nanocubes. *Chem. Mater.* **2003**, *15*, 2829–2835.

(60) Zasada, F.; Grybos, J.; Indyka, P.; Piskorz, W.; Kaczmarczyk, J.; Sojka, Z. Sojka, Surface Structure and Morphology of $\text{M}[\text{CoM}']\text{O}_4$ ($\text{M} = \text{Mg}, \text{Zn}, \text{Fe}, \text{Co}$ and $\text{M}' = \text{Ni}, \text{Al}, \text{Mn}, \text{Co}$) Spinel Nanocrystals - DFT+U and TEM Screening Investigations. *J. Phys. Chem. C* **2014**, *118*, 19085–19097.

(61) Liu, X.; Ma, R.; Bando, Y.; Sasaki, T. High-Yield Preparation, Versatile Structural Modification, and Properties of Layered Cobalt Hydroxide Nanocones. *Adv. Funct. Mater.* **2014**, *24*, 4292–4302.

(62) Ramesh, T. N. Synthesis and thermal stability study of cobalt hydroxynitrate in different polytypic modifications. *Inorg. Chem. Commun.* **2011**, *14*, 419–422.

(63) Xu, Z. P.; Zeng, H. C. Interconversion of Brucite-like and Hydrotalcite-like Phases in Cobalt Hydroxide Compounds. *Chem. Mater.* **1999**, *11*, 67–74.

(64) Sathyanarayana, D. N. *Vibrational spectroscopy: theory and applications*; New Age International Ed.: New Delhi, India, 2004; pp 399–400.

(65) Yang, J.; Liu, H.; Martens, W. N.; Frost, R. L. Synthesis and Characterization of Cobalt Hydroxide, Cobalt Oxyhydroxide, and Cobalt Oxide Nanodiscs. *J. Phys. Chem. C* **2010**, *114*, 111–119.

(66) Hadjiev, V. G.; Iliev, M. N.; Vergilov, I. V. The Raman spectra of Co_3O_4 . *J. Phys. C: Solid State Phys.* **1988**, *21*, L199–L201.

(67) Zhao, X.; Liu, Y.; Wang, J.; Qian, L.; Yao, L.; Chen, Z.; Cai, Q.; Xing, X.; Wu, Z. Modulating the Hydrothermal Synthesis of Co_3O_4 and CoOOH Nanoparticles by H_2O_2 Concentration. *Inorg. Chem.* **2019**, *58*, 7054–7061.

(68) Chellam, U.; Xu, Z. P.; Zeng, H. C. Low-Temperature Synthesis of $\text{Mg}_x\text{Co}_{1-x}\text{Co}_2\text{O}_4$ Spinel Catalysts for N_2O Decomposition. *Chem. Mater.* **2000**, *12*, 650–658.

(69) Olanrewaju, J.; Newalkar, B. L.; Mancino, C.; Komarneni, S. Simplified synthesis of nitrate form of layered double hydroxide. *Mater. Lett.* **2000**, *45*, 307–310.

(70) Deng, D.; Xing, X.; Chen, N.; Li, Y.; Wang, Y. Hydrothermal synthesis of $\beta\text{-Co}(\text{OH})_2$ nanoplatelets: A novel catalyst for CO oxidation. *J. Phys. Chem. Solids* **2017**, *100*, 107–114.

(71) Liu, Z.; Ma, R.; Osada, M.; Takada, K.; Sasaki, T. Selective and Controlled Synthesis of α - and β -Cobalt Hydroxides in Highly Developed Hexagonal Platelets. *J. Am. Chem. Soc.* **2005**, *127*, 13869–13874.

(72) Li, X.; Xu, G.-L.; Fu, F.; Lin, Z.; Wang, Q.; Huang, L.; Li, J.-T.; Sun, S.-G. Room-temperature synthesis of $\text{Co}(\text{OH})_2$ hexagonal sheets and their topotactic transformation into Co_3O_4 (111) porous structure with enhanced lithium-storage properties. *Electrochim. Acta* **2013**, *96*, 134–140.

(73) Leite, E. R.; Ribeiro, C. *Crystallization and Growth of Colloidal Nanocrystals*; Springer: New York, 2012.

(74) Jia, B.-R.; Qin, M.-L.; Li, S.-M.; Zhang, Z.-L.; Lu, H.-F.; Chen, P.-Q.; Wu, H.-Y.; Lu, X.; Zhang, L.; Qu, X.-H. Synthesis of Mesoporous Single Crystal $\text{Co}(\text{OH})_2$ Nanoplate and Its Topotactic Conversion to Dual-Pore Mesoporous Single Crystal Co_3O_4 . *ACS Appl. Mater. Interfaces* **2016**, *8*, 15582–15590.

(75) Gong, M.; Kirkemide, A.; Ren, S. Symmetry-Defying Iron Pyrite (FeS_2) Nanocrystals through Oriented Attachment. *Sci. Rep.* **2013**, *3*, 2–6.

(76) Schwahn, D.; Ma, Y.; Coelfen, H. J. Mesocrystal to Single Crystal Transformation of d,l-Alanine Evidenced by Small Angle Neutron Scattering. *J. Phys. Chem. C* **2007**, *111*, 3224–3227.

(77) Bard, A. B.; Zhou, X.; Xia, X.; Zhu, G.; Lim, M. B.; Kim, S. M.; Johnson, M. C.; Kollman, J. M.; Marcus, M. A.; Spurgeon, S. R.; Perea, D. E.; Devaraj, A.; Chun, J.; De Yoreo, J. J.; Pauzuskie, P. J. A Mechanistic Understanding of Non-Classical Crystal Growth in

Hydrothermally Synthesized Sodium Yttrium Fluoride Nanowires.
Chem. Mater. **2020**, *32*, 2753–2763.